RESEARCH ARTICLE

Key Points:

- New brittle constitutive law describes the onset of faulting in tectonic simulations
- Model is based on sub-critical growth and interaction of micro-cracks
- Laboratory-derived model parameters can be used to model crustal-scale faulting

Correspondence to:
J.-A. Olive,
olive@geologie.ens.fr

Author Contributions:
Conceptualization: Léo Petit, Jean-Arthur Olive, Alexandre Schubnel, Laetitia Le Pourhiet
Data curation: Léo Petit
Formal analysis: Léo Petit, Jean-Arthur Olive, Alexandre Schubnel, Harsha S. Bhat
Funding acquisition: Jean-Arthur Olive, Harsha S. Bhat
Investigation: Léo Petit, Jean-Arthur Olive, Alexandre Schubnel, Laetitia Le Pourhiet, Harsha S. Bhat

A Brittle Constitutive Law for Long-Term Tectonic Modeling Based on Sub-Critical Crack Growth

Léo Petit[1] , Jean-Arthur Olive[1] , Alexandre Schubnel[1] , Laetitia Le Pourhiet[2] , and Harsha S. Bhat[1]

[1]Laboratoire de Géologie, CNRS - École normale supérieure - PSL University, Paris, France, [2]Sorbonne Université, ISTEP, Paris, France

Abstract Adequate representations of brittle deformation (fracturing and faulting) are essential ingredients of long-term tectonic simulations. Such models commonly rely on Mohr-Coulomb plasticity coupled with prescribed softening of cohesion and/or friction with accumulated plastic strain. This approach captures fundamental properties of brittle failure, but is overly sensitive to empirical softening parameters that cannot be determined experimentally. Here we design a brittle constitutive law that captures key processes of brittle deformation, and can be straightforwardly implemented in standard geodynamic models. In our Sub-Critically-Altered Maxwell (SCAM) flow law, brittle failure begins with the accumulation of distributed brittle damage, which represents the sub-critical lengthening of tensile micro-cracks prompted by slip on pre-existing shear defects. Damage progressively and permanently weakens the rock's elastic moduli, until cracks catastrophically interact and coalesce up to macroscopic failure. The model's micromechanical parameters can be fully calibrated against rock deformation experiments, alleviating the need for ad-hoc softening parameters. Upon implementing the SCAM flow law in 2-D plane strain simulations of rock deformation experiments, we find that it can produce Coulomb-oriented shear bands which originate as damage bands. SCAM models can also be used to extrapolate rock strength from laboratory to tectonic strain rates, and nuance the use of Byerlee's law as an upper bound on lithosphere stresses. We further show that SCAM models can be upscaled to simulate tectonic deformation of a 10-km thick brittle plate over millions of years. These features make the SCAM rheology a promising tool to further investigate the complexity of brittle behavior across scales.

1. Introduction

Tectonic plates tend to be almost rigid and primarily deform within narrow boundary zones. In the upper crust (above ~15 km depth), deformation occurs in the brittle regime through nucleation and growth of fractures and faults, which profoundly affect the shape of geological structures and planetary topography. Accurate descriptions of brittle deformation processes are therefore key to answer fundamental questions such as: How and when does a new fault break? How long can it stay active and under what conditions can tectonic stresses reactivate previously active faults? Which mechanisms promote brittle strain localization and modulate off-fault deformation?

Laboratory experiments have long been used to learn about rock deformation mechanisms in the brittle regime (Paterson & Wong, 2005). The brittle behavior of low-porosity crustal rocks (Figure 1) has some defining characteristics. First and foremost, the differential stress that must be applied to break a rock (the rock's strength) increases with pressure (Byerlee, 1967) (Figure 1a, squares and circles). The stress required to slip on a pre-existing discontinuity is also pressure dependent, and both stresses weakly depend on lithology (Byerlee, 1978). The contrast between these two stresses (intact vs. pre-cut) is typically on the order of hundreds of MPas (Figure 1a). Experiments further reveal a number of phenomena that precede macroscopic failure of a rock sample, such as: a reduction of effective elastic moduli, volume expansion, and acoustic emissions (Figures 1b–1d). Failure is a catastrophic phenomenon that occurs when stresses reach a peak strength which is greater when the imposed strain rate is faster (e.g., Lockner, 1998; Paterson & Wong, 2005). Failure manifests as a transition from distributed to localized strain along macroscopic fractures oriented in a systematic manner with respect to the stress field. It is also well documented that rocks can creep when subjected to a constant stress below their peak strength (e.g., Baud & Meredith, 1997; Brantut et al., 2013; Carter et al., 1981; Heap et al., 2009; Kranz, 1979; Figure 1d). Such brittle creep is typically described as involving three phases: A first phase (primary creep) where strain rate decelerates, a prolonged second phase (secondary creep), during which creep rate remains
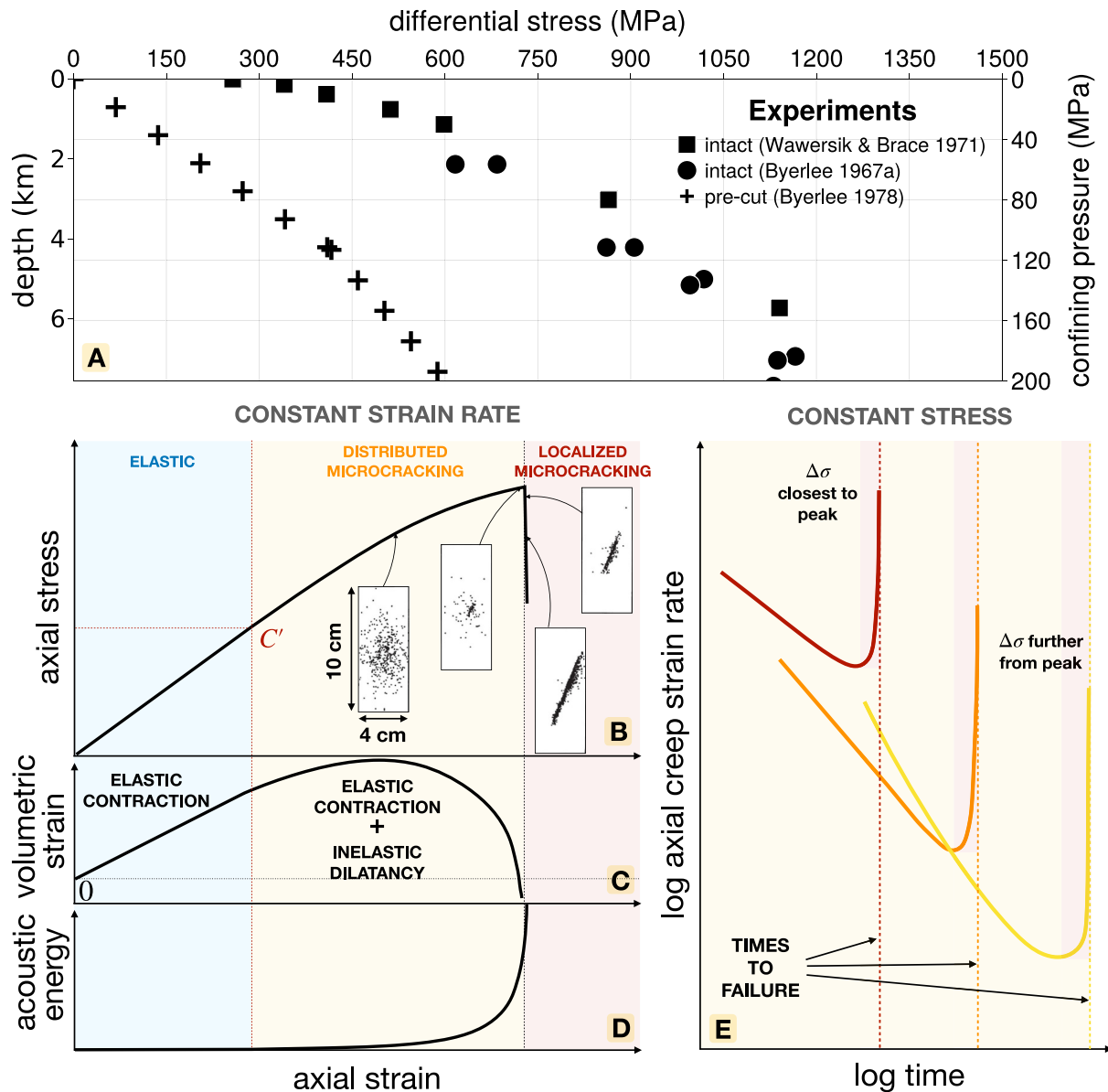
Figure 1. (a) Experimental constraints on brittle rock strength as a function of increasing pressure for intact (squares and circles) and pre-cut (crosses) samples. (b–d) Schematic illustration of axial stress, volumetric strain and acoustic energy versus axial strain, in triaxial experiments performed at a constant strain rate. Point C' marks the onset of dilatancy. Sample cross sections showing the spatial pattern of acoustic emissions are reproduced from Lockner et al. (1991). (e) Typical pattern of axial strain versus time in a brittle creep experiment in which the differential stress $\Delta\sigma$ is imposed and maintained. Colors correspond to values of $\Delta\sigma$ close to (red) or far from (yellow) the rock's peak strength. Here compressive axial strains, strain rates and stresses are plotted as positive numbers for clarity.

nearly steady, and a final stage (tertiary creep) when deformation accelerates until macroscopic failure (Figure 1e, note that the log time representation does not convey the long duration of the secondary phase).

This seemingly complex phenomenology is reasonably well understood as the macroscopic manifestation of the growth and interaction of microcracks that nucleated on pre-existing defects (Tapponnier & Brace, 1976). Crack growth first occurs in a distributed fashion across the sample (Figure 1b). Macroscopic failure then results from the sudden coalescence of interacting microcracks (Figure 1b), whose growth is enabled by differential stress (e.g., Lockner, 1998; Lockner et al., 1991; McBeck et al., 2019). Sample dilatancy points to the tensile nature (mode-I) of some of these cracks, which are susceptible to radiate acoustic energy as they grow (Figure 1d). The time and strain rate dependence of these phenomena further suggests that the speed of crack propagation in the

bulk rock depends on the forces acting at crack tips, which is typical of sub-critical crack growth processes. The main underlying mechanism in the brittle regime is known as stress corrosion (Atkinson, 1984). It refers to reactions occurring between a chemically active fluid and the strained atomic bonds at the tip of microcracks, which induce stress-dependent kinetics of bond breaking (Eppes & Keanini, 2017). While other mechanisms such as pressure-solution (e.g., Gratier et al., 2013), can also contribute to rate-dependent deformation as pressure increases, sub-critical crack growth has been identified as a key contributor to the strain rate (i.e., time-) dependent behavior of brittle rocks in the brittle regime that is particularly well highlighted by brittle creep experiments (Brantut et al., 2013).

Though the phenomenology of brittle failure was well known long before geodynamicists harnessed the power of microprocessors, most tectonic simulations currently rely on a simplified treatment that consists in capping stresses at a rate-independent Mohr-Coulomb yield envelope (e.g., Gerya, 2010; Poliakov & Buck, 1998). This has the advantage of being numerically efficient, adequately capturing the pressure-dependent frictional strength of pre-cut rocks, and spontaneously localizing plastic strain through the bifurcative properties of the Mohr-Coulomb plastic flow rule (e.g., Kaus, 2010; Lemiale et al., 2008; Rudnicki & Rice, 1975; Vermeer & De Borst, 1984). In this framework, strain localization is typically accompanied by a rotation of the principal stresses inside the incipient shear band, which leads to a reduction of the remote stresses (Le Pourhiet, 2013). By itself, this rotation-induced "structural" softening does not account for the 100 s of MPas that separate the strength of intact rocks from their residual strength once faulted (Figure 1a). An approach commonly used to promote sustained strain localization in tectonic simulations (Figure 2) is to weaken the material friction μ and cohesion C, from $\{\mu_{max}, C_{max}\}$ to $\{\mu_{min}, C_{min}\}$ over a certain amount of non-recoverable (plastic) strain Δe_{II}^p (e.g., Lavier et al., 2000; Poliakov & Buck, 1998; Figure 2a). This amounts to enforcing a contrast between intact and broken rocks reminiscent of the strength contrast observed experimentally.

Strain-weakened Mohr-Coulomb plasticity however presents several drawbacks. This parameterization typically ignores the strain rate dependence of rocks' intact strength, and relies on a single value of intact friction and cohesion to determine the intact yield strength. Further, the critical plastic strain Δe_{II}^p is meant to represent a wide range of possible weakening mechanisms, and is therefore not easily quantified through laboratory experiments. These limitations can be problematic since the choice of weakening parameters can have major consequences on the outcome of a tectonic simulation. Lavier et al. (2000) for example, pointed out the spectacular effect of Δe_{II}^p on tectonic styles produced in a rifting simulation (Figures 2b vs. 2c). While some recent studies have investigated the effects of various weakening parameterizations (e.g., Duretz et al. (2021); Meyer et al. (2017); Naliboff
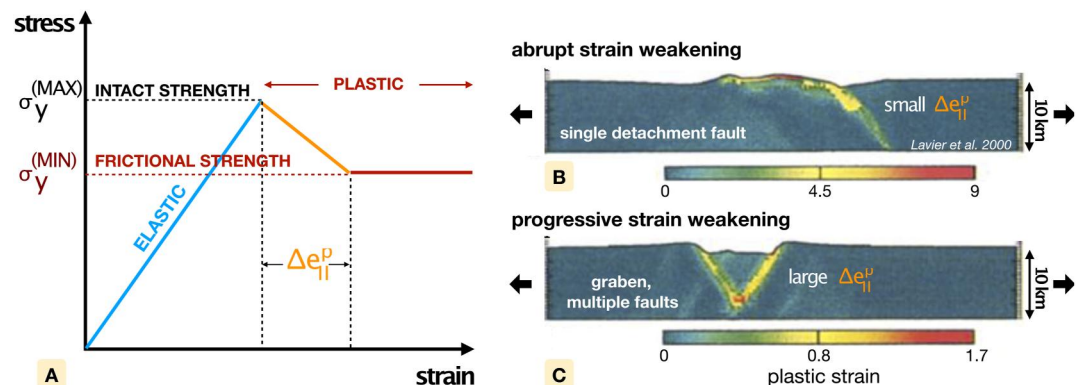
Figure 2. (a) Schematic representation of an elastic-plastic rheology with strain weakening, under constant applied strain rate. The difference between initial $\left(\sigma_y^{(MAX)}\right)$ and final $\left(\sigma_y^{(MIN)}\right)$ yield stresses are caused by a prescribed decrease of frictional properties μ and C over a specified amount of plastic strain Δe_{II}^P. (b–c) Example simulation of extension in a 10 km-thick elastic-plastic upper crust overlying an inviscid medium (Lavier et al., 2000). The only difference between the two panels is the choice of Δe_{II}^P, which is small in b, producing a large-offset normal fault (detachment), and large in c, producing two conjugate faults that outline a graben structure. In this example the difference between $\sigma_y^{(MAX)}$ and $\sigma_y^{(MIN)}$ is caused by a drop in material cohesion while friction is kept constant.

et al. (2020); Pan et al. (2023)), it remains common practice to rely on ad-hoc softening rules in geodynamic simulations without assessing their impact on model behavior.

One path toward remedying this issue is to improve the way geodynamic simulations parameterize the transition from intact to broken rock, in a manner that allows more direct comparison with experimental data and can be interpreted in terms of underlying deformation mechanisms. An adequate parameterization of progressive brittle failure should indeed account for standard observations such as the pre-peak reduction in elastic moduli, the evolving spatial pattern of acoustic emissions, or sample dilatancy which ceases upon failure (Figures 1b–1d). It should also account for the strain rate dependence of brittle yielding and the occurrence of brittle creep. Finally, it should include a representation of the ever-evolving internal state of the rock to include a memory of past deformation events. A promising alternative is to turn to models that describe brittle yielding as the accumulation of damage which ultimately leads to macroscopic failure.

A first family of such models are Continuum Damage Mechanics models. They treat failure as a progressive phenomenon indexed on the alteration of a rock's internal state (damage), and can produce strain rate-dependent brittle strengths, as well as pre-peak softening. Some are built on thermodynamic descriptions of energy dissipation during inelastic deformation (e.g., Hamiel et al., 2004; Karrech et al., 2011; Lyakhovsky et al., 1997), others simply index damage growth on excess stresses above a yield stress, and strain (e.g., Manaker et al., 2006). They do not assume a specific microstructure, which makes them flexible but also not directly interpretable in terms of deformation processes.

In that regard, micromechanics-based models have been particularly successful at capturing the broad range of behaviors associated with brittle deformation (Paterson & Wong, 2005). In this family of damage models, assumptions about the distribution and geometry of pre-existing defects in the material allow the analytical determination of stress concentrations around them, using linear elastic fracture mechanics. Motion along defects cause the stress intensity factors (i.e., a measure of the stress state at the edge of discontinuities) at their tips to increase up to the fracture toughness of the rock, allowing tensile crack propagation. Drivers of such stress heterogeneities can be planar flaws such as grain boundaries, pre-existing microcracks (e.g., Ashby & Sammis, 1990; Kachanov, 1982a, 1982c; Nemat-Nasser & Horii, 1982), pores (Sammis & Ashby, 1986), moduli contrasts across grains in contact (Dey & Wang, 1981), or can even be left undetermined (e.g., Costin, 1985). Tensile cracks, in turn, alter the effective elastic properties of the rock as they lengthen, in an anisotropic fashion (Budiansky & O'connell, 1976; Deshpande & Evans, 2008; Kachanov, 1993; Walsh, 1965a, 1965b). This framework has been used to model high strain rate deformation (e.g., during seismic rupture, Bhat et al., 2012; Thomas et al., 2017) assuming critical fracture propagation, as well as slow deformation assuming sub-critical crack growth (Kachanov, 1982b). The latter class of models has also been used to describe brittle creep, assuming pre-existing planar defects (Brantut et al., 2012), successfully accounting for the multi-phased dynamics of brittle creep (Figure 1e).

One drawback of this approach is its computational cost, because it requires to accurately resolve the kinetics of fracture lengthening, which crack interactions ultimately render unstable close to macroscopic failure. This may explain why it has not yet been implemented in long-term, large scale tectonic simulations, even though the processes it describes are clearly central to the initiation and evolution of crustal faults. By representing specific deformation mechanisms that can be studied in the laboratory, these models can indeed be calibrated against experiments and need not resort to ad-hoc macroscopic parameters (e.g., Bhat et al., 2011; Brantut et al., 2012; Costin, 1983, 1985).

As a first step in this direction, this study aims at constructing a constitutive brittle rheology rooted in the subcritical growth of microcracks from pre-existing rock defects. We seek a formulation that (a) captures the essence of brittle rock behavior at the expense of a few simplifications, (b) has a straigthforward micromechanical interpretation, (c) can be calibrated against experimental data, and (d) is usable in standard 2-D plane strain numerical geodynamic models. We propose such a constitutive law in Section 2, and describe its fundamental behavior in terms of stress-strain curves in Section 3. This allows us to calibrate its parameters using experimental data from both constant strain rate and brittle creep tests. We then implement our constitutive law in 2-D plane strain numerical simulations that reproduce experimental conditions (Section 4), and discuss the model's key features in Section 5. Finally, we implement our constitutive law in a crustal-scale tectonic simulator and compare it to the standard elasto-plastic approach (Section 6).

2. A Sub-Critically Altered Maxwell (SCAM) Constitutive Law for Brittle Deformation

2.1. Generic Stress-Strain Relation

Our constitutive model builds upon an isotropic, incompressible elastic stress-strain relationship:

$$e_{ij} = \frac{s_{ij}}{2G}, \tag{1}$$

linking the deviatoric strain and stress tensors, e_{ij} and s_{ij}, through shear modulus G. In the following, we adopt the convention of summed repeated indices. Our fundamental assumption is that the shear modulus is altered as a function of the internal state of the material, which leads to path-dependent behavior. Specifically, we assume that G decreases as a function of a scalar state variable D, a measure of rock damage, to be defined in Section 2.2:

$$G = G_0\, f(D). \tag{2}$$

In Equation 2, G_0 denotes the shear modulus of the material in its least damaged state, and $f(D)$ a decreasing scalar function of D, hereafter referred to as "weakening function," satisfying $f(D) \in [0,1]$ and $f'(D) < 0$. The incompressible elastic relationship Equation 1 can be recast as a damaged-elastic constitutive law

$$e_{ij} = \frac{s_{ij}}{2G_0\, f(D)}, \tag{3}$$

which takes the form of a Maxwell visco-elastic constitutive law upon time differentiation:

$$\dot{e}_{ij} = \frac{\dot{s}_{ij}}{2G_0\, f(D)} + \frac{s_{ij}}{2\eta_D}. \tag{4}$$

In Equation 4 η_D is a viscosity associated with damage growth:

$$\eta_D = \frac{f^2(D)\, G_0}{|f'(D)|\, \dot{D}}. \tag{5}$$

The damage state variable is related to the lengthening of mode-I microfractures, an intrinsically dilatant process. Throughout this study, inelastic dilatancy is neglected in favor of a purely deviatoric description of the damaged rheology, focusing on the role of microcracking on shear modulus alteration, and on fault nucleation. A strategy to account for damage-induced dilatancy within the SCAM framework will nonetheless be outlined in Section 7. In the following, we detail the micromechanical interpretation of the damage variable, the model governing its growth rate, as well as the weakening function.

2.2. Micromechanical Representation of Rock Damage

Our goal is to model the accumulation of damage in the upper crust, which is primarily composed of low-porosity (<1%) magmatic and metamorphic silicate rocks. These units lie in an overall compressive stress state, with pressures up to hundreds of MPas. Yet, distributed brittle deformation typically involves the opening of mode-I microcracks (Figure 1), which is made possible by stress concentrations around defects or grain boundaries. To describe these processes, we adopt the damage framework developed by Ashby and Sammis (1990) which has been used successfully to predict the brittle strength of several rocks (e.g., Bhat et al., 2011; Baud et al., 2000; X. Wu et al., 2000) at low confining pressure, and the dynamics of fracturing during seismic ruptures (Bhat et al., 2012; Thomas et al., 2017). This model considers the growth of tensile "wing"-cracks from the tips of penny-shaped shear defects distributed within the rock (Figures 3a–3d).

The damage variable represents the relative volume occupied by cracks as the wings lengthen in the direction of the most compressive stress (Figure 3d). It is defined as
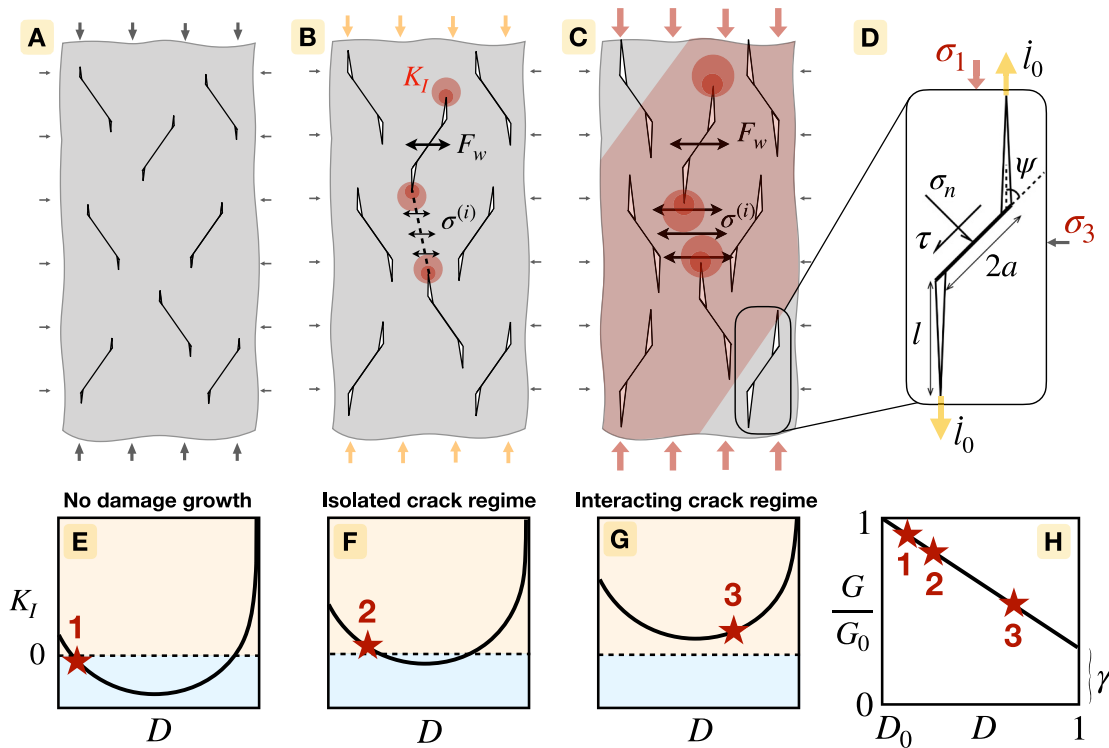
Figure 3. (a–c) Cross-sections in the (σ_1, σ_3) plane showing the array of cracks growing in a rock, in the model of Ashby and Sammis (1990). These cracks initially grow from a shear defect of radius a, oriented at an angle ψ to σ_1. At its tips, "wing" tensile cracks of length l (d) may preexist. Under differential stresses unable to overcome the frictional resistance along shear defects (a), the stress concentration (K_I) at their edges is negative (e) and the material deforms elastically. Once stresses overcome the frictional resistance, the sliding shear defects exert a wedging force F_w increasing K_I (f). Positive K_I promotes stable tensile cracks growth (b). As cracks lengthen, they begin to interact (c). At this point damage growth enters an unstable, accelerating regime (g). (h) Alteration of the shear modulus as a function of damage.

$$D = \frac{4}{3}\pi N_v(\alpha a + l)^3, \tag{6}$$

where N_v is the number of shear defects per unit volume, a and l are the radius of the shear defects and the length of the wing cracks, respectively. $\alpha = \cos\psi$ is the cosine of the angle ψ between the shear defects and the most compressive stress (Figure 3d). The least damaged state ($D = D_0$) corresponds to the state of a rock containing only shear defects, where no wing crack has nucleated (i.e., $l = 0$). The most damaged state occurs at $D = 1$ when the volume of the spheres enclosing each wing crack has grown to match the characteristic volume defined by the spacing of defects ($V_c = 1/N_v$). This upper bound is the result of the formulation of the interaction between cracks, detailed in Section 2.3. It represents a stage at which coalescence of cracks becomes unavoidable. For simplicity, we only consider shear defects with normal vectors lying in the plane of the two extreme principal stresses σ_1 and σ_3. This allows us to index their activity on a 2-D Mohr-Coulomb yield criterion.

2.3. Damage Growth

We assume that under low strain rates and on long time scales, wing cracks lengthen in a sub-critical manner, that is, with stress intensity factors (K_I) lower than the fracture toughness (K_{IC}) of the material (Atkinson, 1984). To capture this process in our constitutive law, we adopt the stress corrosion law introduced by Charles (1958), which has proven successful at explaining experimental data (e.g., Atkinson, 1984; Brantut et al., 2012; Deshpande & Evans, 2008; Kachanov, 1982c). Specifically, the crack growth rate writes

$$\dot{l} = \dot{l}_0\left(\frac{K_I}{K_{IC}}\right)^n, \tag{7}$$

where $\dot{l}_0$ is a characteristic crack growth rate and n the Charles law exponent. The damage growth rate is then retrieved from the wing-crack tip speed

$$\dot{D} = \frac{\partial D}{\partial l}\dot{l} = \frac{3D^{\frac{2}{3}}D_0^{\frac{1}{3}}\dot{l}_0}{\alpha a}\left(\frac{K_I}{K_{IC}}\right)^n. \tag{8}$$

This equation applies only when $K_I > 0$, otherwise $\dot{D} = 0$. Using Equation 7 requires an expression for K_I, the stress intensity factor at the tip of the wing cracks. Following Ashby and Sammis (1990), we assemble K_I as the sum of three terms:

$$K_I = K_I^{(w)} + K_I^{(\sigma_3)} + K_I^{(i)}. \tag{9}$$

The first term $\left(K_I^{(w)}\right)$ represents the stress concentration due to frictional slip on the shear defects wedging open the wing cracks. Following Tada et al. (1973), it can be expressed as the action of a tensile wedging force F_w at the center of an equivalent penny-shaped crack. The radius of this circular crack is that of the sphere enclosing one entire wing crack (shear defect + tensile wings, Figure 3d). However, instead of writing it $l + \alpha a$, as in Equation 6, we write it $l + \beta a$, where β is a regularization factor. This approach was adopted by Ashby and Sammis (1990) to ensure that in the absence of wing cracks ($l = 0$, $D = D_0$), K_I matches the stress intensity factor at the tip of shear defects as derived by Ashby and Hallam (1986). This yields $\beta = 1/\pi$ (Bhat et al., 2011) and the following expression for $K_I^{(w)}$:

$$K_I^{(w)} = \frac{F_w}{[\pi(l + \beta a)]^{3/2}}. \tag{10}$$

The wedging force relates to the excess shear stress acting on the defects (of area πa^2) relative to their frictional resistance. Following Ashby and Sammis (1990), we write:

$$F_w = (\sigma_3 A_3 - \sigma_1 A_1)\, a^2. \tag{11}$$

A_1 and A_3 are constants that depend on the friction and orientation of the shear defects. In the following, we assume $\psi = 45°$ as Ashby and Hallam (1986) showed that this orientation maximizes the wedging force over a wide range of wing crack lengths. This yields:

$$A_1 = \pi\sqrt{\frac{\beta}{3}}\left[\sqrt{1 + \mu^2} - \mu\right] \tag{12}$$

$$A_3 = A_1\left[\frac{\sqrt{1 + \mu^2} + \mu}{\sqrt{1 + \mu^2} - \mu}\right]. \tag{13}$$

Overall, $K_I^{(w)}$ strongly depends on the differential stress $\Delta\sigma = \sigma_3 - \sigma_1$ that develops in the rock, as it allows frictional slip on the defects and wedging of the wings. By contrast, the second term in Equation 9 $\left(K_I^{(\sigma_3)}\right)$ represents remote wing-normal compression σ_3 acting to close tensile cracks. Bhat et al. (2011) estimated it based on results from Tada et al. (1973) as:

$$K_I^{(\sigma_3)} = \frac{2}{\pi}(\sigma_3)\sqrt{\pi l}. \tag{14}$$

Finally, the third term $\left(K_I^{(i)}\right)$ serves to describe the interaction between cracks as they lengthen, and is a core feature of this micromechanical model. Ashby and Sammis (1990) required that the wedging forces applied to cracks be compensated by an internal stress ($\sigma^{(i)}$ in Figure 3) to satisfy mechanical equilibrium. The internal stress is applied on an effective area perpendicular to σ_3 that separates neighboring cracks (A_b). The sum of this area with

the characteristic area of each wing crack ($\pi(l + \alpha a)^2$) amounts to the area A_c that is obtained by projecting the spherical volume $V_c = 1/N_v$ along σ_3. Therefore, $A_b = A_c - \pi(l + \alpha a)^2$, with

$$A_c = \pi^{1/3}\left(\frac{3}{4N_v}\right)^{2/3}. \tag{15}$$

This leads to the following expression for the internal stress acting in the direction of least compression, σ_3^i:

$$\sigma_3^i = \frac{F_w}{A_b}. \tag{16}$$

Internal stress σ_3^i increases dramatically as wings lengthen (D approaches 1) and the areas between fractures (A_b) shrink. This is when crack interactions become dominant. $K_I^{(i)}$ is readily obtained from σ_3^i by analogy with Equation 14:

$$K_I^{(i)} = \frac{2}{\pi}(\sigma_3^i)\sqrt{\pi l}. \tag{17}$$

The full expression of K_I then reads

$$K_I = \frac{F_w}{[\pi(l + \beta a)]^{3/2}} + \frac{2}{\pi}(\sigma_3 + \sigma_3^i)\sqrt{\pi l}. \tag{18}$$

It can be recast as a function of damage rather than crack length, following Bhat et al. (2011), yielding

$$K_I = \sqrt{\pi a}[(\sigma_3 A_3 - \sigma_1 A_1)(c_1 + c_2) + \sigma_3 c_3], \tag{19}$$

where c_1, c_2, and c_3 are functions of the damage state that write

$$c_1 = \frac{1}{\pi^2 \alpha^{3/2}\left[(D/D_0)^{1/3} - 1 + \beta/\alpha\right]^{3/2}} \tag{20}$$

$$c_2 = \frac{2}{\pi^2 \alpha^{3/2}}\left[(D/D_0)^{1/3} - 1\right]^{1/2}\left[\frac{D_0^{2/3}}{1 - D^{2/3}}\right] \tag{21}$$

$$c_3 = \frac{2\sqrt{\alpha}}{\pi}\left[(D/D_0)^{1/3} - 1\right]^{1/2}. \tag{22}$$

2.4. Weakening Function

We next turn to the formulation of the function f(D) used to weaken the shear modulus as damage accumulates. The simplest effective medium representation of a cracked isotropic material assumes non-interacting cracks (Kachanov, 1993). Within this approximation, the change in elastic strain energy due to a population of cracks can be inferred by summing their individual contribution. This amounts to elastic compliances scaling linearly with damage. Elastic stiffnesses therefore scale as $(1 + CD)^{-1}$, where C is a constant that depends on the orientation distribution and geometry of cracks. Linearization of this form provides a reasonable estimate of elastic stiffnesses at low damage values. Because the damage framework of Ashby and Sammis (1990) sets an upper bound on damage at 1, we use this approximation and postulate a linear weakening of G with respect to damage D:

$$f(D) = \frac{\gamma - 1}{1 - D_0}D + \frac{1 - \gamma D_0}{1 - D_0}, \tag{23}$$

such that $G(D_0) = G_0$ and $G(D = 1) = \gamma G_0$. The weakening parameter $\gamma \in [0, 1]$ can be thought of as a property of the material representing the stiffness of a fully damaged rock (e.g., a fault zone) normalized by its maximum possible stiffness in a low-damage state. The derivative of our weakening function with respect to D is:

$$f' = \frac{\gamma - 1}{1 - D_0}. \tag{24}$$

It should be noted that for simplicity our model weakens the shear modulus isotropically, even though damage grows in a highly anisotropic fashion.

To recap, Equations 4 and 5, combined with Equations 8, 19, and 23 make up the complete SCAM constitutive law, which is akin to Maxwell visco-elasticity with a strongly non linear dependence of viscosity on stress, and progressive alteration of the elastic modulus with increasing damage. These equations are reiterated below:

$$\dot{e}_{ij} = \frac{\dot{s}_{ij}}{2G_0\,f(D)} + \frac{s_{ij}}{2\eta_D}$$

$$\eta_D = \frac{f^2(D)\,G_0}{|f'(D)|\,\dot{D}}$$

$$\dot{D} = \frac{3D^{\frac{2}{3}}D_0^{\frac{1}{3}}\dot{l}_0}{\alpha a}\left(\frac{K_I}{K_{IC}}\right)^n$$

$$K_I = \sqrt{\pi a}[(\sigma_3 A_3 - \sigma_1 A_1)(c_1 + c_2) + \sigma_3 c_3]$$

$$f(D) = \frac{\gamma - 1}{1 - D_0}D + \frac{1 - \gamma D_0}{1 - D_0}$$
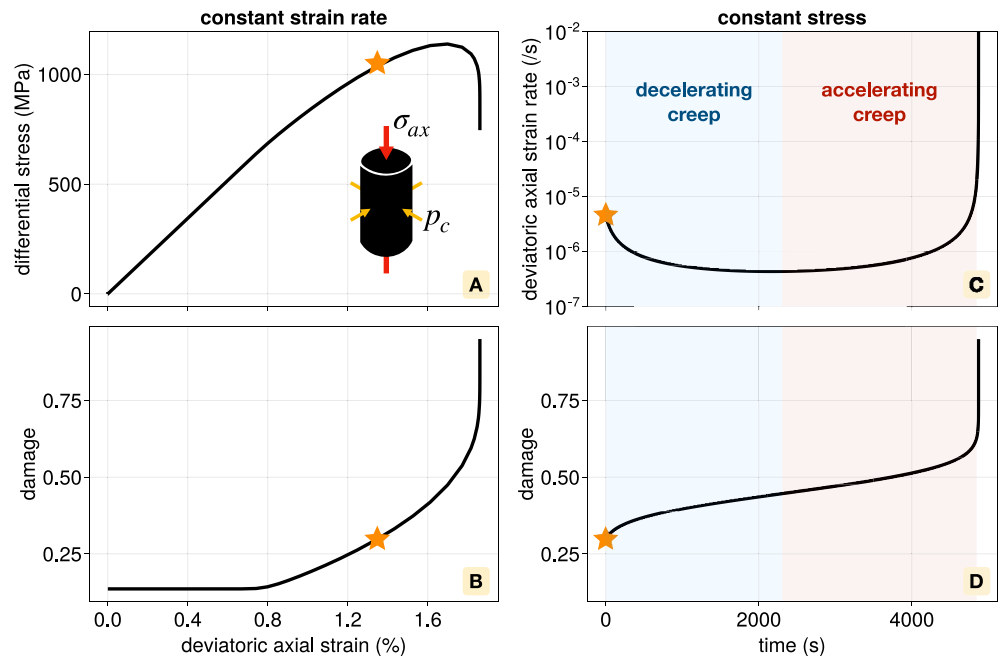
Figure 4. 0-D simulations based on the SCAM model in a typical triaxial setup with a confining pressure of 150 MPa (stress state shown in Panel a). (a and b) Differential stress and damage versus strain in a constant strain rate experiment (10^{-5} s^{-1}). (c and d) Deviatoric axial strain rate and damage versus time in an experiment where stress is kept constant after reaching the stress and damage state pictured by the stars in panels. (a) and (b) Here strains and stresses are represented positive in compression for clarity.

3. Application to a 0-D Triaxial Loading Setup

3.1. Constitutive SCAM Equations in a Triaxial Setup

To illustrate the behavior of the SCAM flow law, we implement it in a geometry typical of rock deformation experiments (Figure 4a): Compression along the axis of a cylindrical sample (σ_1, along direction x_1) subjected to axially symmetric confining stress (σ_3, along directions x_2 and x_3). The corresponding stress tensor writes

$$\underline{\underline{\sigma}} = \begin{bmatrix} \sigma_{ax} & 0 & 0 \\ 0 & -p_c & 0 \\ 0 & 0 & -p_c \end{bmatrix}, \tag{25}$$

where σ_{ax} is the axial stress and p_c the confining pressure surrounding the curved surface of the sample. We use a simplified point-wise formulation of our differential constitutive relationship Equation 4 assuming homogeneous deformation within the sample. As stated previously, we ignore volumetric strain and focus solely on the relationship between the deviatoric axial strain rate $\dot{e}_{ax}$ and the deviatoric axial stress s_{ax}. The constitutive equations reduce to the following ordinary differential equation (ODE):

$$\dot{e}_{ax} = \frac{\dot{s}_{ax}}{2G_0\, \mathrm{f}(D)} + \frac{s_{ax}}{2\eta_D}, \tag{26}$$

to be solved jointly with the damage evolution equation (Equation 8).

A first type of experiment consists of applying a constant axial strain rate and measuring the axial stress. In our framework, s_{ax} verifies:

$$\dot{s}_{ax} = 2G_0\, \mathrm{f}(D)\left(\dot{e}_{ax} - \frac{s_{ax}}{2\eta_D}\right), \tag{27}$$

with $s_{ax}(t=0) = 0$ and $D(t=0) = D_i \geq D_0$.

Another class of experiments (brittle creep tests) consists of applying a constant axial stress and measuring the axial strain. In our model, the latter is given by

$$\dot{e}_{ax} = \frac{s_{ax}}{2\eta_D}, \tag{28}$$

In this case, the initial value of D cannot be chosen arbitrarily and must be consistent with the imposed stress. To ensure this, we first integrate the constant strain rate and damage growth ODEs (Equations 8 and 27) up to the desired value of axial deviatoric stress s_{ax} assuming a known strain rate. The damage value reached at the end of this preliminary step is used as initial condition for Equations 8 and 28, along with $e_{ax}(t=0) = 0$. These equations are integrated up to D close—but not equal—to 1, due to the singular behavior at this limit, coming from the c_2 term in Equation 21.

The above ODEs are integrated numerically using a 5/4th order Runge-Kutta method (Tsitouras et al., 2009). This is done within the DifferentialEquations.jl Julia package (Rackauckas & Nie, 2017) using adaptive time-stepping with absolute and relative tolerance of 10^{-6} and 10^{-4} respectively.

3.2. Stress-Strain Curves and Creep Regimes

We illustrate the fundamental behavior of the SCAM model in triaxial experiments using reference micromechanical parameters appropriate for Westerly granite (Table 1), which will be rigorously determined in Section 3.3. Constitutive equations are integrated up to $D = 0.95$.

Figures 4a and 4b correspond to a constant strain rate setup at $10^{-5}\ \mathrm{s}^{-1}$, under 150 MPa of confining pressure. The axial stress-strain curve displays an initial elastic phase followed by visible weakening of the effective modulus when differential stress exceeds $\sim$700 MPa. This is accompanied by damage growth (Figure 4b) which

Table 1
Inverted Parameters

Symbol	Description	Westerly granite	Darley Dale sandstone
G_0	Shear modulus at $D = D_0$ (GPa)	28.72 ± 0.02	5.202 ± 3
γ	Residual ratio G/G_0 at $D = 1$	0.432 ± 0.004	0.281 ± 0.003
μ	Friction coefficient of the shear flaws	0.703 ± 0.001	0.5093 ± 0.0003
a	Shear flaws radius (μm)	6.66 ± 0.16	656.8 ± 4.3
n	Charles law exponent	11.82 ± 0.03	24.96 ± 0.07
$\dot{l}_0$	Charles law reference crack growth rate (mm s^{-1})	16.44 ± 0.19	0.0029 ± 0.0001
K_{IC}	Fracture toughness (MPa m$^{1/2}$)	1.29 ± 0.01	1.412 ± 0.004
D_0	D associated to the shear flaws only	0.1358 ± 0.0003	0.3724 ± 0.0008
D_i	Initial value of D	0.1361 ± 0.0003	0.27 ± 0.05

accelerates catastrophically as the sample reaches its peak stress. The post-peak stress drop is similarly abrupt as damage approaches 1.

Figures 4c and 4d correspond to a constant stress simulation starting at the yellow star shown in panels A and B. Strain rate first decelerates, then remains steady for hours, and ultimately accelerates up to the macroscopic failure of the material, consistent with the subsequent phases of brittle creep observed experimentally (Figure 1e). What is usually referred to as secondary creep would here be associated to the transition between decelerating and accelerating creep, and was not depicted in Figures 4c and 4d because of the clear bimodal dynamics of brittle creep expressed by the SCAM model. This strain rate behavior is associated with dynamics similar to those of the damage growth rate, visible through the slope of damage evolution with respect to time in Figure 4d.

The effect of various model parameters and experimental conditions on the behavior of the SCAM model under constant strain rate is shown in Figure 5. The black curves correspond to a strain rate of 10^{-5} s^{-1}, a confining pressure of 150 MPa and the reference set of micromechanical parameters for Westerly granite (Table 1). Figures 5a and 5b shows that a reduction of the imposed axial strain rate leads to a lower peak stress due to damage having more time to accumulate under lower axial stress, precipitating failure (Figure 5b). Increasing the radius of the shear defects (Panel e) while keeping D_0 constant leads to a decrease of the peak stress. This is because the stress intensity factor at the wing crack tips increases with increasing shear defect size, prompting faster crack growth. Thus, significant damage can build under lower stresses, and the peak stress is reached sooner. Increasing D_0 while keeping the shear defect size constant (Panel f) also leads to a lower peak stress, but limits the amount of softening that takes place pre-peak. This is because cracks arranged in a denser array will interact and coalesce sooner. The stress decrease additionally does not display the abrupt drop seen with the reference case, which we attribute to the larger reduction of shear modulus per damage increment. A decrease of the Charles law exponent n (Panel g) or friction coefficient (Panel d) similarly lowers the peak stress, by enabling damage build-up under lower stress intensity factors Equation 7 and under lower differential stress, respectively. Finally, a greater degree of modulus weakening (via a reduced γ parameter) leads to more pre-peak softening but has a limited impact on the peak stress (Panel h). It also stabilizes the stress drop by limiting the unstable growth of damage as it gets close to 1. In this case of extreme loss of elastic stiffness, the larger negative stress increment associated with damage increment post-peak tends to reduce the catastrophic increase in damage growth.

To better visualize the dynamics of damage growth in the SCAM model, we represent constant strain rate experiments in a plot of differential stress versus damage (Figure 6a). This representation allows us to map the stress intensity factor at the wing-crack tip (colors and contours in panel a), which gives us a proxy for damage growth rate. We specifically highlight two sets of experiments. The first set is performed at a laboratory strain rate $\dot{\varepsilon}_{ax} = 10^{-5}$ s^{-1}, and the second at a tectonic strain rate of 10^{-15} s^{-1}, both under a confining pressure $p_c = 150$ MPa. In each set, we vary the initial damage D_i, using values of 0.136 (D_0), 0.227, 0.318, 0.409, and 0.5.

Each experiment follows a specific trajectory in differential stress versus damage space. For example, in the case of no initial tensile cracks ($D_i = D_0$), differential stress first increases while damage remains constant. This is because in the initial elastic regime, $K_I <= 0$ and wing cracks cannot grow. Once the system reaches the domain of positive K_I, damage can start growing, and increases with stress. The system appears to follow a contour of
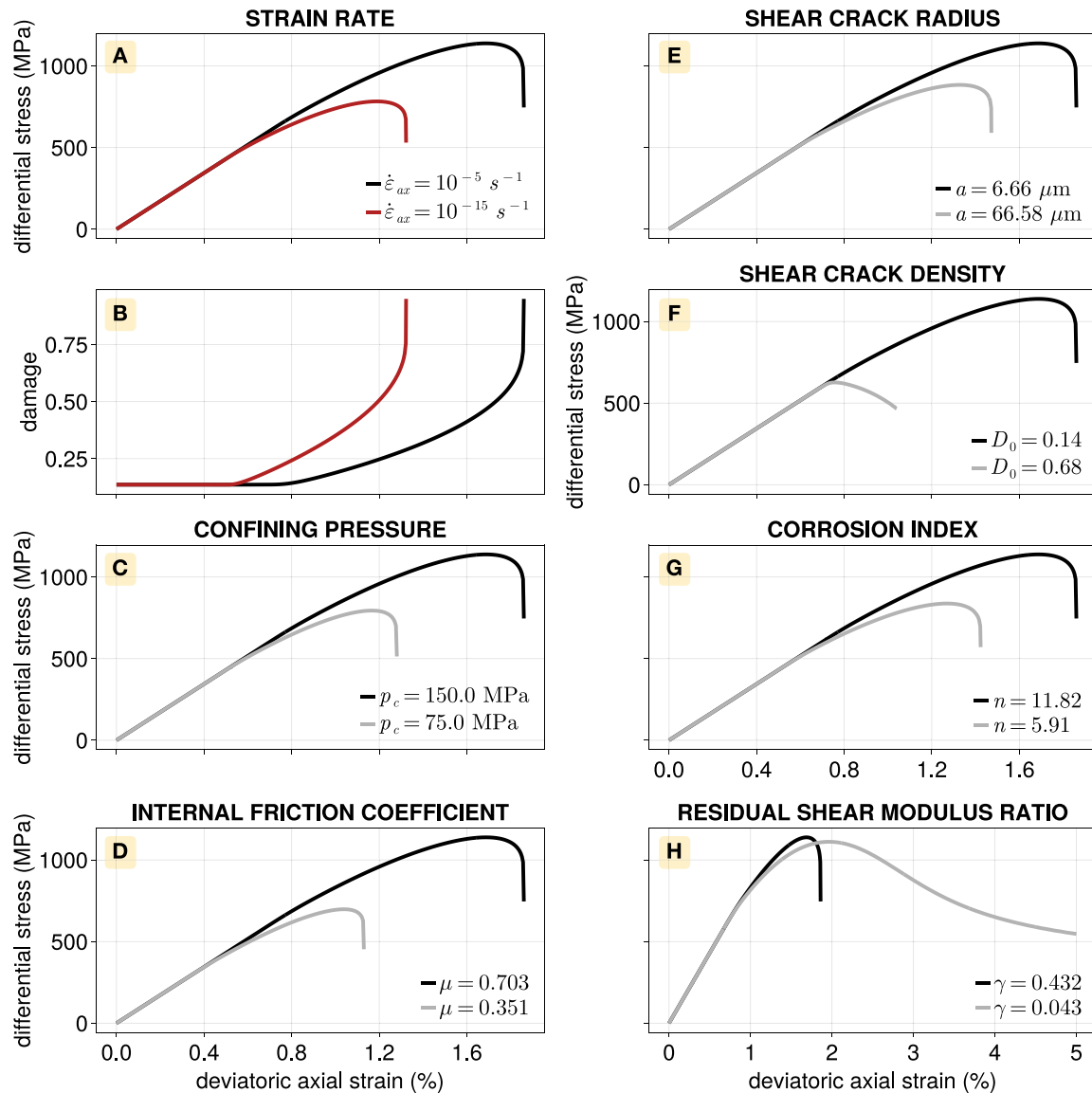
Figure 5. Effect of strain rate (a), (b), confining pressure p_c (c), friction coefficient μ (d), shear defect radius a (e), shear crack density D_0 (f), corrosion index n (g) and residual shear modulus γ (h) on differential stress with respect to deviatoric axial strain for 0-D SCAM simulations. Black lines correspond to the best fitting parameters for Westerly granite detailed in Section 3.3. Here strains and stresses are represented positive in compression for clarity.

constant K_I up to the peak differential stress ($\sim$1,140 MPa). Past this point, the differential stress starts to decrease while damage keeps increasing at an accelerating pace. This is due to the fact that K_I, which sets the rate of damage growth, now increases with increasing damage. This final phase of rapid failure manifests as an abrupt post-peak stress drop in the stress-strain curve (Panel b).

These three regimes, characterized by the absence of growth, the stable and then the unstable growth of damage is illustrated in Figure 3 with the three numbered stars respectively. Simulations carried out under the same strain rate, but with greater initial damage show the same behavior, and their trajectories tend to align along the same iso-K_I ($\sim$0.3K_{IC}) path as followed by the $D_i = D_0$ case. This forms an envelope that materializes an upper bound of the differential stress value with respect to damage. This envelope corresponds to ($K_I \sim 0.05 K_{IC}$) for tectonic strain rates, and therefore lies at lower stress values. If, however, a simulation is initiated with damage in excess of $\sim$0.45 (e.g., orange paths in panel A), damage will immediately start growing in the unstable regime, where $\partial K_I/\partial D > 0$. In this case, the system reaches a peak stress which is lower than that of the other simulations.
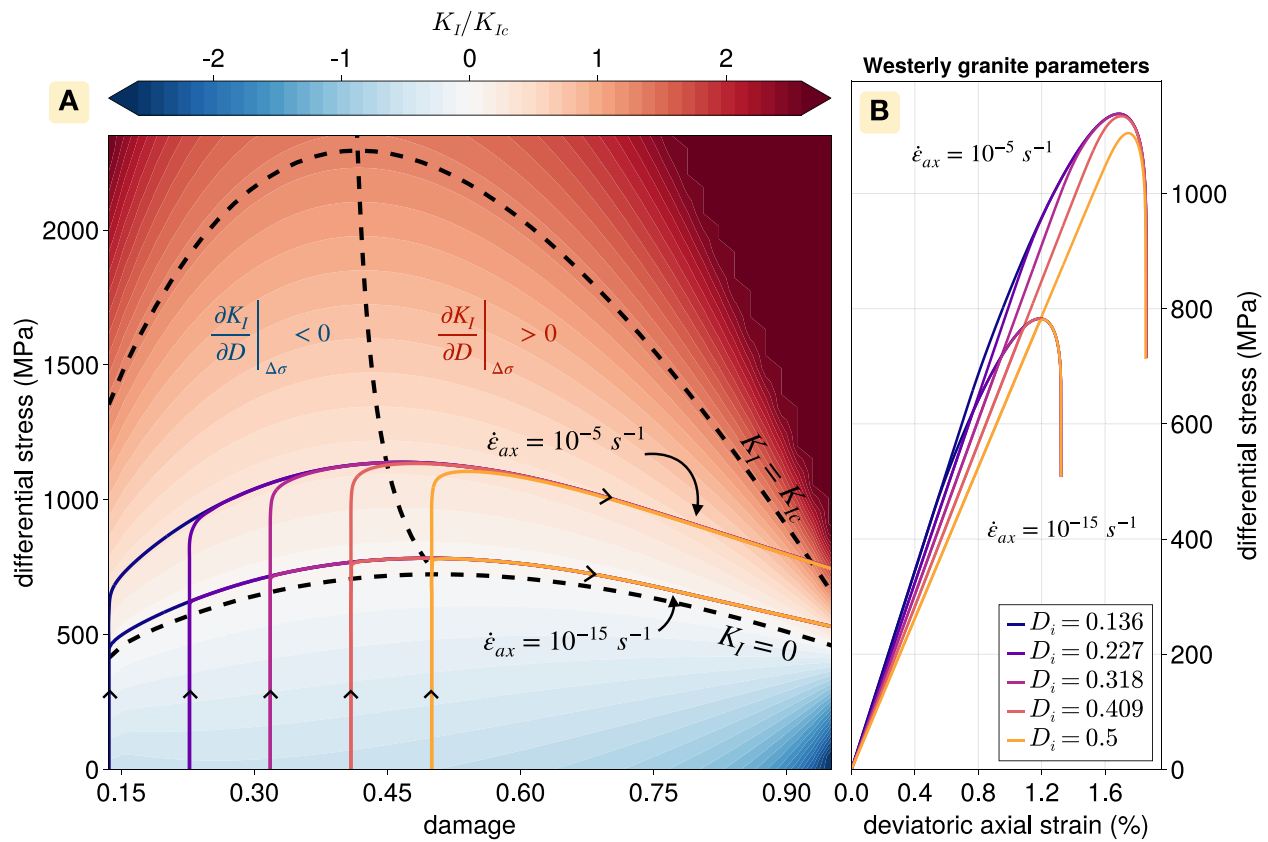
Figure 6. (a) Trajectories of differential stress with respect to damage at $\dot{\varepsilon}_{ax} = -10^{-5}$ s^{-1} and $\dot{\varepsilon}_{ax} = -10^{-15}$ s^{-1} for various initial damages (color code) and at constant confining pressure $p_c = 150$ MPa. The background is colored according to K_I/K_{IC}, with the two iso-values pictured with black dashed contours representing $K_I = 0$ and $K_I = K_{IC}$ respectively. The near-vertical dashed black line highlights damage values where $\partial K_I/\partial D = 0$ under constant $\Delta\sigma$. (b) Same trajectories plotted as standard deviatoric axial strain versus differential stress, along with the color code for initial damage state. Strains and stresses are represented positive in compression for clarity.

3.3. Calibration of SCAM Parameters With Laboratory Experiments

The ability of the SCAM model to reproduce both constant strain rate and constant stress experiments suggests that laboratory data can be used to constrain its micromechanical parameters (Table 1). Specifically, stress-strain curves from constant strain rate experiments under various confining pressures can help constrain elastic and frictional properties, while strain rates and time to failure in brittle creep tests contain information about the kinetics of damage build-up.

To leverage this information, we use the 0-D "forward" models presented in the previous section in a Bayesian inversion framework (Tarantola, 2005, see Appendix A for details). We expect 0-D models to be representative of the homogeneous deformation stage up to the peak stress (prior to localization), as micro-cracking is known to first develop in a distributed fashion (Figure 1).

3.3.1. Experimental Data

We apply the Bayesian inversion method to experimental data corresponding to two lithologies. The first is Westerly granite, a rock type widely used in experiments that is representative of the continental upper crust in term of mineralogy and low porosity. This rock has been shown to experience the type of diffuse cracking and catastrophic fracture coalescence that our model seeks to capture (e.g., Lockner et al., 1991; Tapponnier & Brace, 1976). We specifically use constant strain rate $\left(\dot{\varepsilon}_{ax} = 10^{-5}\mathrm{s}^{-1}\right)$ experiments under confining pressures of 20, 30, 80, and 150 MPa in dry conditions from Wawersik and Brace (1971) (Figure 7a). We complement these data with minimum brittle (secondary) creep strain rates measured under seven imposed differential stresses ranging from 77% to 93% of the short-term strength (meaning the peak strength at a laboratory strain rate) of the
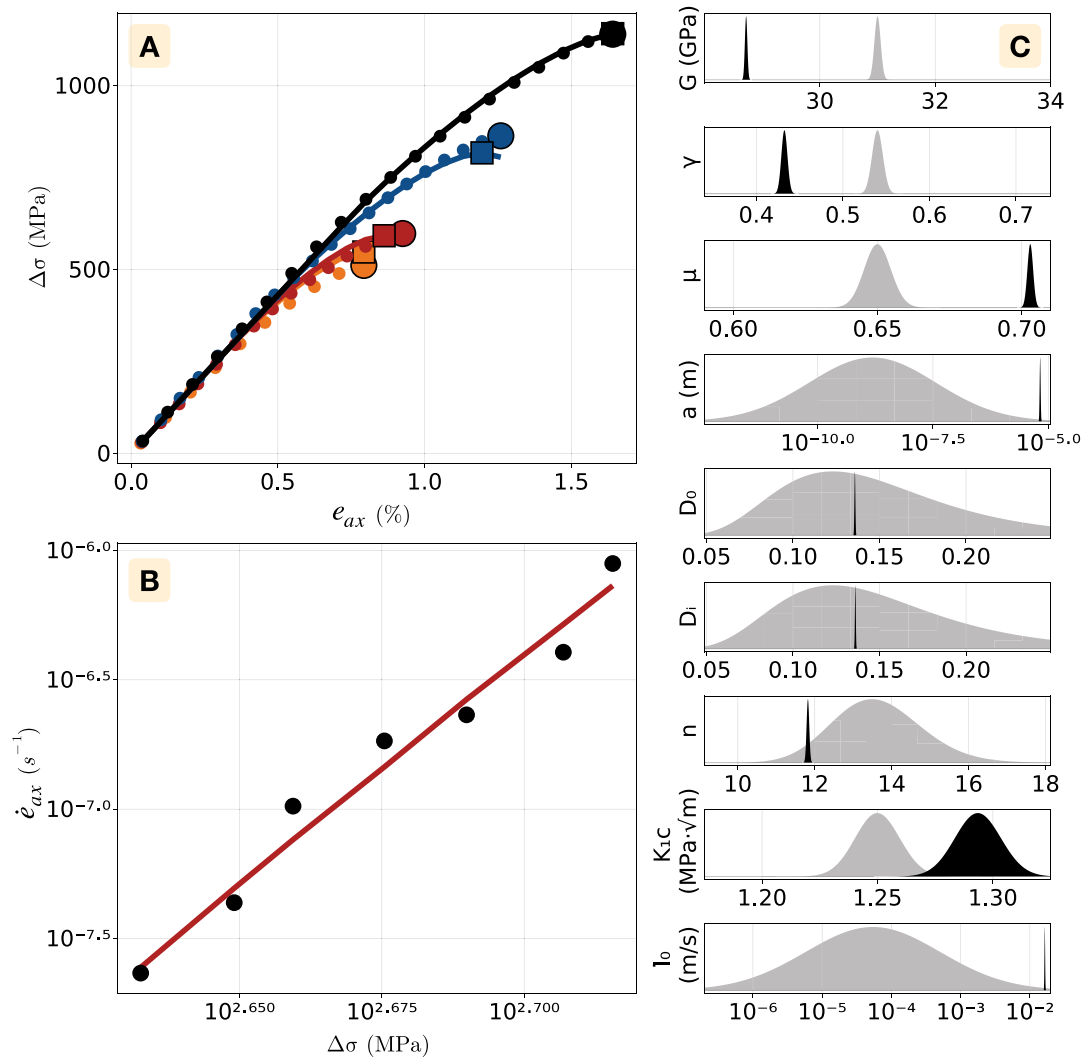
Figure 7. SCAM model fit to experimental data on Westerly granite. (a) Constant strain rate experiments with $\dot{\varepsilon}_{ax} = -10^{-5}$ s^{-1} and confining pressures of 20 (orange), 30 (red), 80 (blue) and 150 MPa (black). Dots show the data and lines the best fitting models. (b) Dataset of minimum brittle creep strain rate as a function of imposed differential stress (black dots), with relationship derived from best fitting model (red line). (c) Prior (gray) and posterior (black) distributions of inverted micromechanical parameters.

rock subjected to an effective confining pressure of 30 MPa in water-saturated samples by Brantut et al. (2012) (Figure 7b).

The second rock type we consider is Darley Dale feldspar-rich sandstone, another widely studied lithology. While its properties are likely less representative of the upper crust than that of Westerly granite, inferring its micromechanical parameters can provide helpful comparisons to assess the validity of our model. One caveat of this choice is that porous sandstone may deform according to mechanisms other than the growth of tensile cracks from shear defects, such as Hertz-contact driven microfracturing (e.g., Zhang et al., 1990), tensile cracks nucleating from pores (e.g., Sammis & Ashby, 1986), or distributed cataclastic flow where microcracking grows along grain boundaries (e.g., Menéndez et al., 1996). Heap et al. (2009) however report that for confining pressures up to their maximum of 50 MPa, stress-induced damage grows predominantly in a direction subparallel to the axis of compression. Additionally, dilatancy patterns at constant strain rate are very similar to what is observed in low-porosity rocks such as Westerly granite (e.g., X. Wu et al., 2000; Zoback & Byerlee, 1975). These observations suggest that the wing-crack model remains a relevant conceptual framework for the brittle deformation of Darley Dale sandstone, at least below 50 MPa of effective confining pressure.

Friction coefficient μ, fracture toughness K_{IC} and pre-existing crack length a were previously estimated for Darley-Dale by X. Wu et al. (2000) within the Ashby and Sammis (1990) wing-crack framework, but assuming critical crack growth (i.e., at $K_I = K_{IC}$). Here, we additionally use entire time series of brittle creep strain rates from Heap et al. (2009) to provide strong constraints on the kinetics of crack growth. We specifically use experimental results performed under constant stresses of 80%, 85% and 90% of the short-term strength from Heap et al. (2009) (Figure 8b). We combine these time series with stress-strain curves determined under a constant strain rate of 10^{-5} s^{-1} and confining pressures of 10 and 50 MPa in water-saturated samples from the same authors (Figure 8a). While data was also available for a confining pressure of 30 MPa, it displayed a significantly different shear modulus compared to the other two. We thus decided to exclude it from the joint inversion procedure.

It should be noted that because our constitutive law is based on incompressible elasticity, we remove the volumetric component of elastic deformation (i.e., the Poisson effect) from constant strain rate experimental data. In
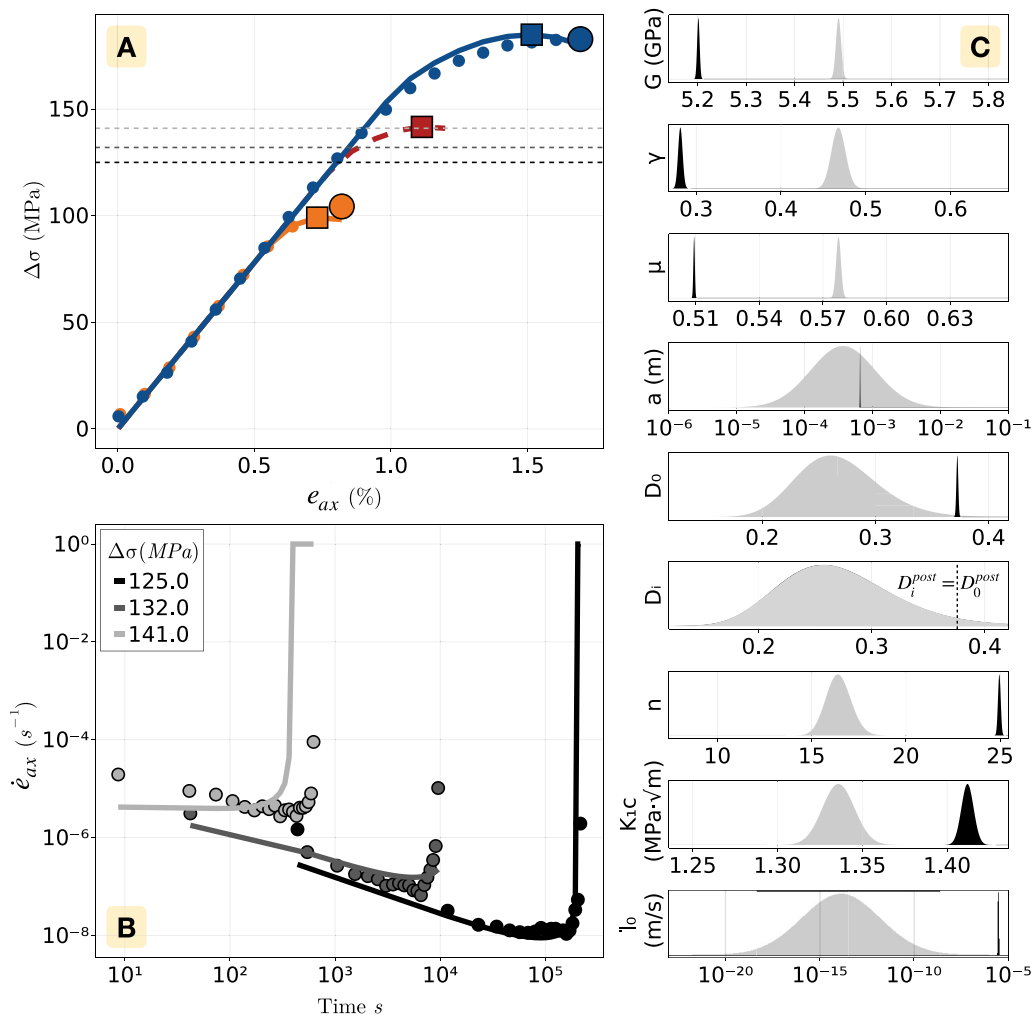

Figure 8. SCAM model fit to experimental data on Darley Dale sandstone. (a) Constant strain rate experiments with $\dot{\varepsilon}_{ax} = -10^{-5}$ s^{-1} and confining pressures of 10 (orange) and 50 MPa (blue). Dots show the data and lines the best fitting models. Larger circles and squares indicate experimentally determined and modeled peak stress, respectively. Horizontal dashed lines show the imposed stress levels for the experiments shown in Panel (b). (b) Brittle creep tests shown as time series of axial strain rate under imposed differential stress and confining pressure $p_c = 30$ MPa (dots and lines correspond to data and models, respectively). A simulated constant strain rate curve at this confining pressure is included in Panel a (red dashed curve with red square marking the peak stress). (c) Prior (gray) and posterior (black) distributions of inverted parameters. The posterior distribution of the initial damage state D_i is the same as its prior because the inversion kept lowering the D_i value to below D_0, which was not permitted. This resulted in a null gradient of the log-likelihood with respect to D_i and thus no change of the parameter nor of its posterior distribution relative to the prior.

practice, this means that the reported strain rate is converted to a deviatoric axial strain rate $\dot{\varepsilon}_{ax}' = \frac{2}{3}(1 + \nu)\dot{\varepsilon}_{ax}$, with ν the Poisson's ratio, in order to compare our simulations with laboratory results.

3.3.2. A-Priori Parameters

The a-priori value of G is chosen based on the initial slope of the elastic (linear) portion of available stress-strain curves. The initial value of the friction coefficient μ is set to the standard value of 0.65 (Byerlee, 1978). We initially assume K_{IC} to fall between values determined experimentally in quartz (1 MPa $\cdot$ $m^{1/2}$) and wet Westerly granite (1.74 MPa $\cdot$ $m^{1/2}$) from the compilation of Atkinson (1984). We initialize γ at an intermediate value of 0.5, and a at the mean grain size of Westerly granite: 0.5 mm. We also set $D_0 = D_i$ at 0.2, $n = 12$ (Atkinson, 1979), and $\dot{l}_0 = 10^{-2}$ m s^{-1}. This set of a-priori guesses on the parameter values is first used to invert only the data from constant strain rate experiments. The results of this step are used to construct new priors on the model parameters, shown as gray shadings in the right columns of Figures 7 and 8. These priors are then used for a combined inversion of constant strain rate and brittle creep experiments, using a step multiplier $\kappa = 0.1$ (See Appendix A for details). A hundred steps were typically sufficient to reach convergence, yielding the posterior model parameter distributions shown in black in the right column of Figures 7 and 8.

3.3.3. Results

Figure 7 shows the results of our joint inversion of constant strain rate and brittle creep data in Westerly granite. Panel a compares the SCAM-simulated stress-strain curves (plain lines) and the experimental data points. The agreement is good at confining pressures of 30, 80, and 150 MPa. At 20 MPa, however, the model slightly overestimates the peak stress. The Wawersik and Brace (1971) study also contains data at atmospheric, 3.5 and 10 MPa confining pressures, but under these conditions our model was not able to accurately represent the pressure dependence of the peak stress. Figure 7b also shows secondary creep strain rates as a function of imposed differential stress from our simulations (red line), which are in good agreement with experimental data (black dots). The relationship between brittle creep strain rate and stress is effectively a power law with a stress exponent of ~18.

The best fitting parameter values as well as their log-normal standard deviations are listed in Table 1, and shown as probability distributions (in black) in Figure 7. Because the prior distributions (in gray) were determined by fitting only constant strain rate data, the differences between prior and posterior distributions highlight the information provided by brittle creep data. This information specifically constrains the initial damage state, as well as parameters related to the kinetics of damage growth such as $\dot{l}_0$ or n. It also strongly constrains the size of shear defects (to ~7 μm), which influences K_I and therefore the damage growth rate. Parameters such as K_{IC}, μ and γ are also slightly re-evaluated.

Best-fitting stress-strain curves for Darley Dale sandstone are shown in Figure 8a for 10 and 50 MPa of confining pressure as plain lines, along with experimental data (points). Larger markers mark the peak stress of simulations (squares) and experiments (circles). The red dashed line shows an additional simulated curve at an intermediate pressure of 30 MPa. This pressure corresponds to that of the brittle creep tests (Figure 8b), which were conducted under three axial stresses indicated as dashed lines in Figure 8a. It can be seen that the greatest applied differential stress (141 MPa) is very close to the inferred peak stress at 30 MPa of confining pressure. Figure 8b compares simulated and measured strain rates in the brittle creep experiments. Our best fitting parameters do a good job at reproducing the shape of the strain rate curves as well as the time to macroscopic failure (the final, near-vertical portion of the curves).

Similarly to our results in Westerly granite, joint inversions of brittle creep tests and constant strain rate experiments provide strong constraints on parameters such as shear defect size, initial damage, Charles law exponent, and $\dot{l}_0$. Our inversions yield a significantly greater defect size (~700 μm vs. ~7 μm) and Charles law exponent (~25 vs. ~12) in sandstone compared to granite, as well as a lower shear modulus and greater degree of elastic weakening (lower γ). The initial damage state of sandstone also appears greater. We however find comparable fracture toughness in both lithologies, and a slightly greater coefficient of (defect-scale) friction in granite (0.7 vs. 0.5).

4. Application to a 2-D Plane-Strain Numerical Press

4.1. Conservation Equations and Numerical Methodology

In order to perform 2-D simulations of material deformation governed by the SCAM constitutive equations, we adapt the long-term tectonic modeling code *SiStER* (Simple Stokes solver with Exotic Rheologies, Olive et al. (2016)), which solves for conservation of mass, momentum (and energy if needed), in a 2-D continuum assuming elastic incompressibility and planar deformation. Conservation of mass and momentum write:

$$\frac{\partial v_i}{\partial x_i} = 0, \tag{29}$$

and

$$\frac{\partial s_{ij}}{\partial x_j} - \frac{\partial P}{\partial x_i} + \rho g_i = 0, \tag{30}$$

where v_i are velocities, $P = -1/3 \, \sigma_{kk}$ is pressure, ρ is density and g_i the gravitational acceleration. Deviatoric stresses s_{ij} are related to velocities in Equation 30 using a Maxwell visco-elastic constitutive relationship between deviatoric stresses and strain rates (e.g., Gerya, 2010; Moresi et al., 2003):

$$\dot{e}_{ij} = \frac{1}{2G}\dot{s}_{ij} + \frac{1}{2\eta}s_{ij} \tag{31}$$

where $\dot{s}_{ij}$ is discretized using a first-order backward finite difference scheme with time step Δt, so that the deviatoric stress at time t becomes

$$s_{ij}^t = 2Z\eta\dot{e}_{ij}^t + (1-Z)s_{ij}^{t-\Delta t}, \tag{32}$$

with $\dot{e}_{ij} = (\partial v_i/\partial x_j + \partial v_j/\partial x_i)/2$ and

$$Z = \frac{G\Delta t}{\eta + G\Delta t}. \tag{33}$$

The effective viscosity in Equation 31 can represent a range of rheologies. A very high value sets a very long Maxwell time, which effectively renders the material elastic. In the viscous regime, η can represent brittle plasticity (e.g., as detailed in Section 4.2.2), or a specific creep mechanism of known flow law. In practice, η is constructed as the harmonic average of several viscosities, each representing individual flow mechanisms.

The mass Equation 29 and momentum Equation 30 conservation equations, expressed in terms of velocities Equation 32 and pressure, are discretized with a conservative finite difference scheme formulated on a staggered grid (e.g., Gerya & Yuen, 2003). This leads to a linear system that is solved for velocities and pressure over the entire domain using a direct solver. Retroactions between the viscosity and velocity fields require the use of non-linear iterations (here approximate-Newton, described as Algorithm 2 in Spiegelman et al. (2016)) to reach convergence, which is assessed by comparing the L2 norm of the residual vector to a specified tolerance (relative tolerance between 10^{-7} and 10^{-2}, see *readme* documentation in the code repository linked in the Acknowledgments section).

Once a reasonably converged solution is found, the time evolution is performed explicitly using the time step Δt introduced in Equation 32. This is specifically done by advecting Lagrangian markers which carry material properties such as density, viscosity and friction. Markers are advected within the velocity field interpolated from the nodes. Marker properties are then passed back to the nodes to prepare the next solve of the conservation equations at the next time step. Markers also carry material stresses in order to solve Equation 32. In addition to being advected, these stress components are also rotated according to the local rotation rate determined from the velocity field at each timestep (Gerya, 2010).

4.2. Numerical Implementation of the SCAM Rheology

The implementation of the SCAM model in the 2-D code was performed as described in the following sub-sections. First, a damage property and its evolution rules are implemented, along with the shear modulus dependence on damage. Then, a smooth transition to long term plastic behavior in fully damaged parts of the material is introduced.

4.2.1. Damage Growth and Viscosity

The damage state D is added as an additional variable discretized on both markers and nodes. Its evolution Equation 8 is solved with a finite difference method. The damage rate $\dot{D}$ and its associated viscosity η_D (Equation 5) are evaluated on nodes at each non-linear iteration using previous stresses and interpolated damage values from markers. The shear modulus is also altered according to the damage state.

When stepping through time, marker damage is incremented by interpolating the damage rate from nodes to markers. Due to the non-linearity of Equation 8, damage is prone to catastrophic growth, which can be challenging for a numerical solver. We therefore adapt the time step to the dynamics of damage growth by limiting the maximum increment of damage on a node at each time iteration by an amount $\Delta D_{\max}$.

4.2.2. Switching From Damaged to Plastic Rheology After Crack Coalescence

D values approaching 1 can be thought of as a state when the rock looses its macroscopic cohesion through crack coalescence. Our damage rheology is not well suited to represent large strains that may develop beyond this point, for example, within localized fault zones. Mohr-Coulomb plasticity, on the other hand, is perfectly relevant to model the frictional rheology of such fault gouges. Crack coalescence is however a necessary condition to the formation of macroscopic fault zones, such that damage growth up to 1 has to precede Mohr-Coulomb plastic deformation. Our damage model being formulated as an effective Maxwell rheology, we choose to retain this framework in our implementation of plasticity. We therefore implement a continuous effective viscosity that smoothly switches from our damage viscosity η_D to the standard plastic viscosity η_P (Duretz et al., 2021) as D approaches 1.

Because in our micromechanical model crack normals lie in the $\{\sigma_1, \sigma_3\}$ plane, plastic deformation beyond coalescence should be confined to that same plane, and can therefore be modeled with a Mohr-Coulomb yield criterion ensuring that

$$s_{II} \leq \sigma_y, \tag{34}$$

where $s_{II} = \sqrt{J_2(\sigma)}$, with $J_2(\sigma) = 1/2\ s_{ij}s_{ij}$ the second invariant of the deviatoric stress tensor. s_{II} is also the radius of Mohr's circle in 2-D incompressible plane strain:

$$s_{II} = \frac{1}{2}(\sigma_3 - \sigma_1). \tag{35}$$

In Equation 34, the plastic yield stress σ_y writes:

$$\sigma_y = \sin\phi_m\ P + \cos\phi_m\ C_m. \tag{36}$$

The yield stress is a function of the macroscopic friction angle $\phi_m = \arctan\mu_m$ and cohesion C_m, as well as of the in-plane pressure P:

$$P = -\frac{1}{2}(\sigma_1 + \sigma_3), \tag{37}$$

which in elastically incompressible 2-D plane strain is also equal to total pressure. Satisfying the Mohr-Coulomb yield criterion within a Maxwell visco-elastic framework can be done through an effective "plastic viscosity" approach (e.g., Gerya (2010); Duretz et al. (2021)). As fully damaged areas become incompressible elastic-plastic zones, Equation 4 becomes:

$$\dot{e}_{ij} = \frac{\dot{s}_{ij}}{2G_0\,\mathrm{f}(D)} + \frac{s_{ij}}{2\eta_p}. \tag{38}$$

The plastic viscosity η_p is set to guarantee that stresses satisfy the Mohr-Coulomb criterion Equation 34 once "broken" material starts behaving as a plastic fault zone. If s_{II} lies below σ_y, η_p is effectively infinite (plasticity is not activate), otherwise η_p reads (see Appendix B):

$$\eta_p = \frac{s_{II}}{2\left(\dot{e}_{II} - \frac{\sigma_y - s_{II}}{2G_0\,\mathrm{f}(D)\Delta t}\right)}, \tag{39}$$

where $\dot{e}_{II} = \sqrt{J_2(\dot{e})}$ is the second invariant of the strain rate tensor. A smooth transition from damage to plastic viscosity is implemented using a hyperbolic tangent function $\mathrm{S}(x)$ that goes from 0 to 1 as its argument goes from negative to positive. We set the lowest viscosity to the plastic viscosity and thus write the continuously differentiable effective viscosity:

$$\eta_{eff} = \mathrm{S}(\eta_D - \eta_p)\eta_D + (1 - \mathrm{S}(\eta_D - \eta_p))\eta_p. \tag{40}$$

To ensure that the effective viscosity remains plastic when material is fully damaged, we set $\eta_D(D = 1)$ to the smallest viscosity that can be resolved by our numerical solver (see Section 4.3).

Including the transition to large-strain plasticity, the complete set of differential equations that constitute the SCAM model can be summarized as

$$\dot{e}_{ij} = \frac{\dot{s}_{ij}}{2G_0\,\mathrm{f}(D)} + \frac{s_{ij}}{2\eta_{eff}}. \tag{41}$$

When subjected to loading, the material first responds elastically with $D = D_i$ (its initial damage state $\geq D_0$), until K_I becomes positive and damage starts growing (Figure 3). At that moment damage-driven alteration of the shear modulus generates an effective damage viscosity which affects the material behavior. Up to peak stress, the damage viscosity is greater than the plastic viscosity since it allows stress build-up, therefore $\eta_{eff} \sim \eta_D$. During the post-peak stress drop, η_D quickly drops below the plastic viscosity which then becomes the effective viscosity. This allows the accumulation of large strains under stresses capped by the Mohr-Coulomb yield stress. Said yield stress is computed according to Equation 36. In the following, we adopt a macroscopic friction angle that matches the frictional properties of the shear defects, that is, $\phi_m = \tan^{-1}\mu$. We also assume that the fully damaged material is cohesionless, that is, $C_m = 0$. It should be noted that a fully damaged material may also return to an elastic behavior if s_{II} happens to drop below σ_y. However, its shear modulus will have been permanently reduced by damage ($G = \gamma G_0$).

4.3. 2-D Setup: The Numerical Press

We construct a 2-D plane-strain analog to the triaxial experimental setup described in Section 3, following the geometry shown in Figure 9. This allows us to simulate constant strain rate deformation of a Westerly granite sample, with micromechanical properties determined in Section 3.3 (Table 1), up to large strains and including localization. The axial symmetry of triaxial tests allows us to only consider half of the sample's cross-section. Our geometry thus consists of a half-sample 10 cm tall and 2 cm wide on the right side of a wider box (10.5×6 cm) that includes confining fluid left of the sample, and a 0.5 mm-thick "piston" above the sample (Figure 9). Constant strain rate conditions are enforced by pushing material inward from the top of the domain at a constant velocity. The piston is here to ensure that new material flowing in during deformation is not of sample type. Outward velocities are prescribed along the left boundary to preserve a constant volume in the computational domain. The confining fluid is modeled as a low-viscosity Newtonian medium, with pressure imposed at the lower left corner of the domain. Gravity is ignored. The initial sample damage fluctuates spatially between $D_i = 0.136$ and 0.236 with an isotropic Perlin noise structure that represents material heterogeneities. The spatial domain is discretized using cell sizes of 2×0.5 mm within 3 cm of the left wall, and 0.5×0.5 mm within 3 cm of the right wall, that is, the part of the domain containing the sample.
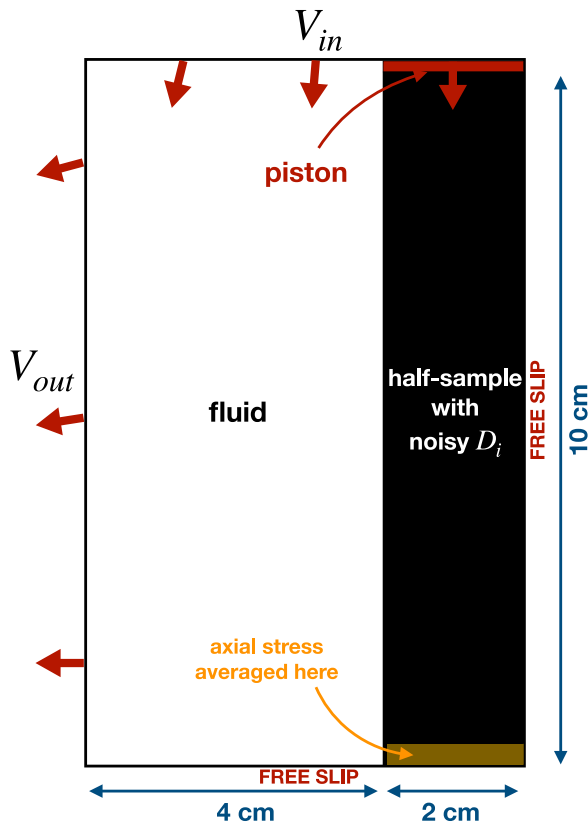
Figure 9. Geometric setup used to simulate experimental deformation in 2D plane-strain. Exploiting the axial symmetry of triaxial experiments, we only model the left-half of a cross section containing the sample axis. The half-sample has a length of 10 cm and a width of 2 cm. It is initially seeded with a noisy damage field. A small piston one cell tall (with the same mechanical properties as the sample) is pushed in above the sample. Left of this assemblage lies the confining fluid kept at a constant pressure. Top and left borders are associated with Dirichlet boundary conditions on the velocity component normal to the borders, while the tangential components are left free. The right and bottom borders are free slip. Axial stress is evaluated by averaging vertical stresses in a 0.5 cm thick slice at the bottom of the sample.

The convergence of Stokes solvers being very sensitive to viscosity contrasts, we restrict the maximum variation in viscosity across the domain to five orders of magnitude. We do so by setting an upper bound on viscosity $\eta_{\max}$ such that its associated Maxwell time $\eta_{\max}/G$ is 50 times longer than the time required to elastically reach the peak stress at the imposed axial strain rate. This large viscosity is initially assigned to the sample, rendering it effectively elastic at the beginning of the simulation. A lower bound on viscosity in the numerical domain is obtained through $\eta_{\min} = 10^{-5} \times \eta_{\max}$. This low viscosity is assigned to the confining fluid, ensuring that it behaves viscously throughout the simulation. Because the damage viscosity η_D drops significantly as damage accumulates, the effective viscosity of the sample will decrease as it begins to fail. As η_D approaches η_p, a smooth transition toward plastic viscosity is performed over a viscosity range $|\eta_D - \eta_p| \approx \eta_{\min}/50$. Regardless of the viscosity transition, damage keeps increasing until reaching 1. At this point, it stops evolving and η_D is fixed at $\eta_{\min}$. Once parts of the sample are fully damaged, they effectively behave as a Mohr-Coulomb plastic solid with no cohesion and the same (macroscopic) friction coefficient as that determined to act on the microscopic shear defects (0.7).

Finally, the comparisons of simulated constant strain rate experiments with laboratory data requires the evaluation of macroscopic axial strains and deviatoric stresses. The axial strains are measured by tracking the displacement of the top boundary of the sample through time, and normalizing it by the initial size of the sample. Axial deviatoric stresses are obtained by averaging the vertical deviatoric stress s_{ax} in a horizontal "stress gauge," that is, a 0.5 cm thick band at the bottom of the numerical sample (Figure 9), excluding a cell size length near the left boundary, to avoid any influence from interpolations at the interface between sample and fluid.

4.4. Results

Figure 10 shows results from the numerical press performed under a constant axial strain rate of 10^{-5} s^{-1} (Panels a and b) and 10^{-15} s^{-1} (Panel b), and confining pressures of 30, 80, and 150 MPa. Figure 10c illustrates the patterns of damage growth and plastic strain for the simulation performed under 150 MPa of confining pressure (black lines in Panels a and b), on the left and right halves of each snapshot, respectively. The timing of each snapshot is indicated by the numbers on the stress-strain curve in Panel b. Up to snapshot 3, damage grows in a distributed fashion, which smoothes the initial heterogeneities. Damage increases homogeneously up to ~0.45 during that stage. Just prior to the peak stress, damage growth starts to localize close to the sample border, forming fast-growing damage bands at angles of ~30° with respect to the compression direction. They develop within a strain range of less than 0.01% (snapshots 5, 6, 7). Plastic strain is estimated by integrating the second invariant of the inelastic deviatoric strain rate tensor through time (once Mohr-Coulomb plasticity has been activated), and accumulates within fully damaged bands. Plastic shear banding first lags behind damage banding. Once a sample-scale damage band has grown, it effectively becomes a plastic shear band. This process begins as the axial stress drops abruptly (snapshots 6–7). Interestingly, off-band distributed damage does not evolve significantly during shear band development.

Figure 10a compares the stress-strain curves produced in our 2-D simulations to the experiments of Wawersik and Brace (1971) described in Section 3.3, performed under the same conditions. To facilitate comparisons between a 2-D plane strain and an axisymmetric setup, we normalize the differential stress $\Delta\sigma = \sigma_3 - \sigma_1$ by its value at $K_I = 0$ and $D = D_0$, which is the criterion for the onset of tensile crack growth (even though the crack growth rate is infinitely slow at $K_I = O^+$):
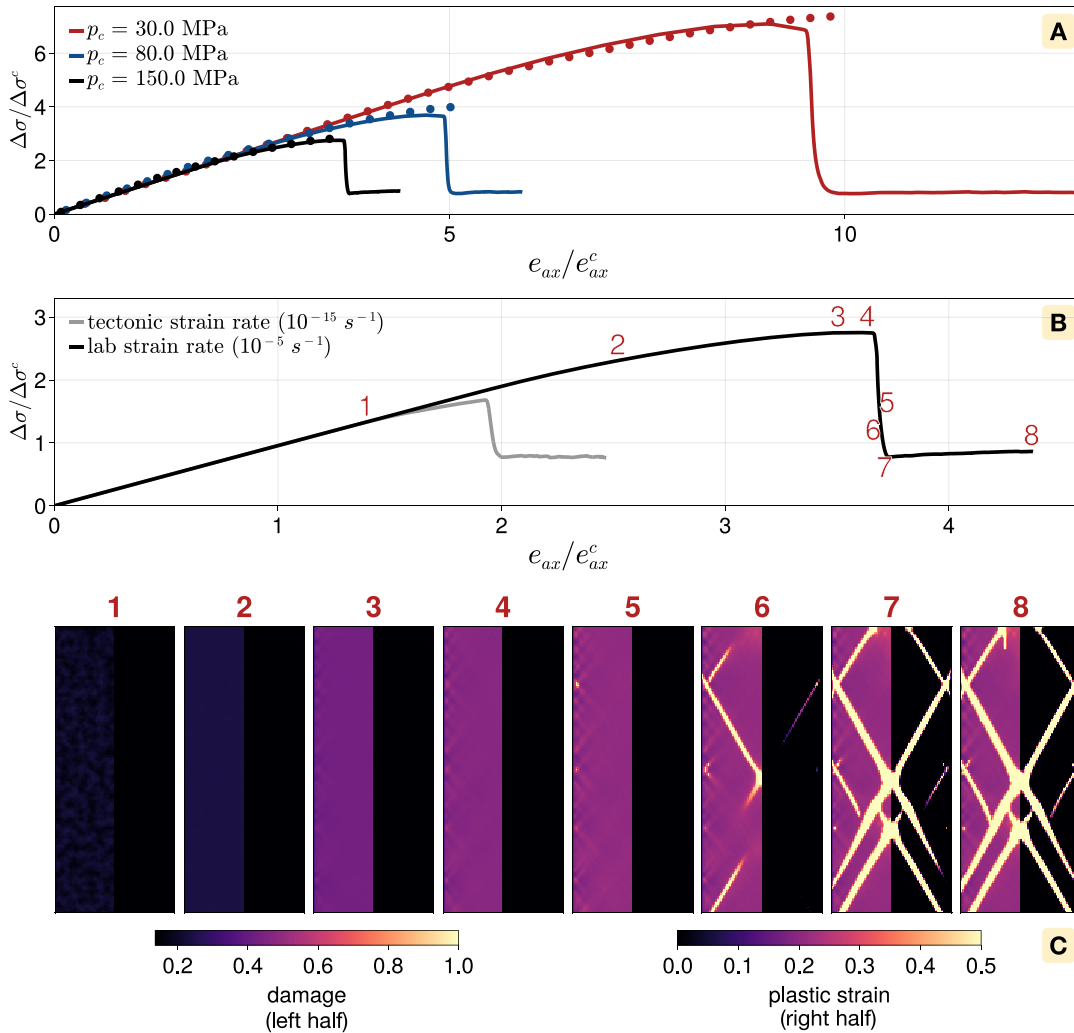
Figure 10. Results of the SCAM model simulations in a 2-D plane-strain setup using Westerly granite parameters under constant strain rate. The numerical samples are initialized with a noisy D_i field. (a) Simulated stress-strain curves at $\dot{\varepsilon}_{ax} = -10^{-5}$ s^{-1} and confining pressures of 30 (red), 80 (blue) and 150 MPa (black curve), to be compared with the corresponding experimental data (dots). (b) Simulation performed at $p_c = 150$ MPa described above compared to a simulation at a "tectonic" strain rate of 10^{-15} s^{-1}. Differential stresses and deviatoric axial strains are normalized by their value when $K_I = 0$ at $D = D_0$ to allow comparison between triaxial experimental data and 2-D plane strain deformation (see Text). The red numbers in Panel b correspond to the damage (left) and plastic strain (right) snapshots shown in Panel (c).

$$\Delta\sigma^c = p_c\left(1 - \frac{\sqrt{1+\mu^2} + \mu}{\sqrt{1+\mu^2} - \mu}\right) \tag{42}$$

The above expression is obtained by applying the Mohr-Coulomb criterion to optimally oriented planes in a principal stress field. The axial deviatoric strain is then normalized by the deviatoric strain needed to reach $\Delta\sigma^c$ elastically with the reference shear modulus G_0 that corresponds to $D = D_0$:

$$e_{ax}^c = \frac{1}{2G_0}s_{ax}^c. \tag{43}$$

In Equation 43, s_{ax}^c is the deviatoric axial stress at the onset of microcraking, and is equal to $\Delta\sigma^c/2$ in a 2-D plane strain configuration, and to $(2/3)\Delta\sigma^c$ for a triaxial configuration. This non-dimensionalization of stresses and strains accounts for the fact that the mean stress, which impacts damage growth and the position of the peak stress, has a different expression in a triaxial versus plane-strain geometry. It ensures that experiments conducted with

the same parameters in either geometry will show the same non-dimensional tangent modulus and peak differential stress.

Our 2-D simulations are in good agreement with the experimental data from Wawersik and Brace (1971) (Figure 10a) at all three confining pressures. This shows that the parameters determined by fitting 0-D (pointwise) simulations to triaxial data produce sensible behavior when implemented in a 2-D "spatialized" geometry. Figure 10b shows our reference simulation at $\dot{\varepsilon}_{ax} = 10^{-5}$ s^{-1} and $p_c = 150$ MPa in black, compared to a simulation performed at a "tectonic" strain rate of 10^{-15} s^{-1}. The peak stress of the slower simulation is significantly lower than that of the reference simulation, with a loss of strength during macroscopic failure that is approximately divided by 2.

5. Discussion: A Brittle Constitutive Law Rooted in Micromechanics

5.1. Features of Brittle Deformation Captured by the SCAM Model

As illustrated in Sections 3 and 4, the SCAM model captures a range of features typical of brittle deformation revealed by laboratory experiments (Figure 1). These include: (a) the co-existence of several measures of rock strength, such as the intact strength and the residual (i.e., "pre-cut") frictional strength, all of which depend on confining pressure (e.g., Byerlee (1978)); (b) the permanent weakening of elastic properties occurring prior to the peak stress; (c) the strain rate-dependence of brittle strength, which enables (d) the occurrence of brittle creep under constant imposed stress. Here we discuss the parameters of the SCAM framework that control these various macroscopic properties.

5.1.1. Microscopic Versus Macroscopic Strength, Elastic Weakening, and Strain Rate Dependence

The SCAM framework involves several thresholds of inelastic deformation. The first is when slip on pre-existing, small-scale shear defects becomes able to wedge open tensile wing cracks. It corresponds to $K_I = 0$ (Figures 3 and 6), and is closely related to the Mohr-Coulomb criterion, in the sense that opening wing cracks requires a greater differential stress under greater confining pressure (Costin, 1985). The second threshold is when cracks have sufficiently lengthened to transition from a non-interacting to an interacting regime. This aspect will be further detailed in Section 5.1.2. The third threshold is when D reaches its maximum value ~ 1, at which point cracks coalesce into a macroscopic fault, which is modeled as a shear band with a macroscopic "bulk" friction equal to that acting on the microscopic shear defects, and no cohesion. In practice, the second and third thresholds occur in very close succession because the damage growth rate accelerates catastrophically as soon as cracks enter the interacting regime, especially under constant axial strain rate. Some amount of deformation is still required for the shear band to reach its steady-state stress after the third threshold (e.g., after snapshot 7 in Figure 10). After that, the macroscopically broken rock has a "residual" strength that is entirely set by its friction coefficient.

The material's elastic properties are altered by damage, causing pre-peak softening of the rock and permanent weakening of the shear modulus. The ratio of the fully damaged $\left(V_s^D = V_s(D = 1)\right)$ over the reference $\left(V_s^0 = V_s(D = D_0)\right)$ shear-wave velocity can be related to the shear modulus weakening ratio γ, assuming small density variations, as: $V_s^D / V_s^0 \approx \sqrt{\gamma}$. Using γ values inverted from Westerly granite and Darley Dale sandstone (Table 1) we obtain shear-wave velocity reductions of 34% and 47%, consistent with values measured in the damage zone of natural faults, which range from 20% to 50% (e.g., Karabulut & Bouchon, 2007; C. Wu et al., 2009), as well as laboratory tomography on granite showing a reduction in P-wave velocity of around 50% (Aben et al., 2019).

The SCAM model accounts for the temporal dependence of brittle deformation via a sub-critical crack growth law, which allows cracks to grow below the fracture toughness of the material (Costin, 1983, 1985). This assumption introduces a characteristic crack growth time $a/\dot{l}_0$ that is modulated by the stress intensity factor (K_I) and the Charles law exponent n (Equation 7). These parameters themselves depend on ambient conditions such as moisture levels (Atkinson, 1979; Eppes & Keanini, 2017) or temperature (Heap et al., 2009). To first order, the strain rate dependence of the SCAM flow law reflects the ratio of the characteristic duration of the deformation of interest to the characteristic crack growth time. A very slow ("tectonic") experiment will for example, leave ample time for cracks to grow, weaken the material and cause macroscopic failure, preventing the build-up of very large stresses (Figure 10b). Conversely, experiments conducted under laboratory strain rates will reveal greater peak

stress (e.g., Figure 7 of Costin (1983)). Interestingly, the strain rate dependence of brittle deformation implies that wide portions of the upper crust should behave in an effectively viscous fashion (with viscosity η_D) when undergoing progressive failure (i.e., prior to localization). This behavior must however be inherently transient because the amount of damage a rock can withstand before macroscopic failure is necessarily finite. A competition between crack growth and crack healing processes may prolong this distributed viscous deformation phase, but is beyond the scope of the present study.

5.1.2. Retroactions Between Damage and Damage Growth Rate

The transition between a regime of lengthening but non-interacting wing cracks, and one of catastrophically interacting long cracks (Figure 3) is at the heart of many macroscopic behaviors manifested by the SCAM model. As detailed in Section 2.3, the stress intensity factor (K_I) at the tip of wing cracks is constructed as the sum of three terms (Equation 9). The first two terms lead to a decrease in K_I as wing cracks lengthen, that is, as D increases. This corresponds to the isolated crack regime. The third term has the opposite effect: increasing D increases K_I, and thus the damage growth rate through Charles' law (Equation 7). This last term becomes dominant at larger values of D and describes the interacting crack regime. The transition between successive regimes is closely related to the convexity of K_I as a function of D, and its dependence on the evolving differential stress, as illustrated in Figures 3e–3g.

In constant strain rate experiments, damage starts to grow when K_I becomes positive. This is made possible by elastic loading raising the differential stress at constant initial damage state D_i (vertical trajectories in Figure 6). When an experiment is started with a low D_i, damage growth first occurs in the non-interacting regime, where $\partial K_I/\partial D < 0$ (e.g., purple trajectory in Figure 6). Damage growth rates are initially very slow, because K_I/K_{IC} raised to a large exponent (n in Equation 7) gives an extremely slow crack growth speed when K_I barely exceeds 0. The damage viscosity is initially very high, and the material continues to behave elastically. As damage increases, both the shear modulus and the damage viscosity decrease because of the decreasing f(D) and $f^2(D)$ terms in Equations 2 and 5. This leads to pre-peak softening of the stress-strain curve. The crack growth rate—strongly controlled by K_I—is the sole mechanism that can lead to a stress rate decrease. It thus competes with the elastic stress rate increase imparted by far-field loading, controlling the stress level at which material softening occurs. In Figure 6, this manifests as trajectories aligning on a contour of constant K_I, which is greater for a greater imposed strain rate.

Then, the system transitions to the interacting regime where $\partial K_I/\partial D > 0$. The regime transition as illustrated in Figure 6a connects all the differential stress maxima spanning all values of K_I between 0 and K_{IC}. We write D_c the "critical" damage value that marks this regime transition. D_c decreases with increasing differential stress (vertical black dashed curve in Figure 6a), and verifies:

$$\left.\frac{\partial K_I(D)}{\partial D}\right|_{D=D_c(\Delta\sigma)} = 0. \tag{44}$$

Because prior to crossing the regime transition stress trajectories align close to an iso-K_I contour (which depends on strain rate), the value of D_c can be thought of as a decreasing function of strain rate. D_c is bounded by the value of damage that maximizes the differential stress at $K_I = K_{IC}$ (here ~0.42), and the value that maximizes stress at $K_I = 0$ (here ~0.5). These end-member cases respectively represent a very fast strain rate experiment, in which cracks would grow critically (at elastic wave speeds), and an extremely long and slow experiment in which cracks can grow sub-critically at $K_I \sim 0$. The upper and lower bound on D_c happen to be close to each other, yielding a narrow range of critical damage values (~$0.42 - 0.5$ in Figure 6a). When damage exceeds D_c, the system enters the interacting regime, in which an increase in D increases $\dot{D}$ at constant stress, thereby accelerating the reduction of the shear modulus (Equation 2) and damage viscosity η_D (Equation 5). The material can no longer accumulate stress, and stresses decrease below their peak value. At this point the stress trajectories in Figure 6a begin to deviate from an iso-K_I. For our best-fitting set of parameters, K_I increases drastically as D exceeds D_c, which manifests as a sharp stress drop as D approaches 1 (Figure 6).

An interesting consequence of the fact that pre-peak stress trajectories tend to first align on the same iso-K_I contour regardless of initial damage state is that they all experience a regime transition at the same D_c and at the same peak differential stress (for a given imposed strain rate). In Figure 6b, this manifests as peak stress

magnitudes that are largely insensitive to any value of initial damage lower than D_c. This feature of the model is consistent with experimental results from Wang et al. (2013), who found similar peak strength in samples initially subjected to varying degrees of thermal cracking, which we interpret to represent varying D_i (i.e., varying wing crack lengths at fixed shear defect size and density). On the other hand, if an experiment is started with a damage state that exceeds D_c, the system will entirely bypass the non-interacting regime and will display very little post-peak softening (e.g., light orange trajectories in Figure 6a). In this case, the degree of initial damage affects the position of the peak stress.

We note that in a few instances, large values of damage do not lead to a catastrophic stress drop. This occurs for example, for low values of γ (Figure 5h), or a high value of D_0 (Figure 5f), where stresses slowly decay over a few percent of axial strain. The only way to prevent a catastrophic stress decrease is for K_I to decrease as D approaches 1. In Figure 6a, this would manifest as a steeply decreasing stress trajectory that crosses iso-K_I contours for $D > D_c$. The slope of a stress trajectory in $(D, \Delta\sigma)$ space is equal to $\frac{\partial \Delta\sigma}{\partial D} = \frac{3}{2} \frac{\dot{s}_{ax}}{\dot{D}}$. Post peak, the deviatoric axial stress rate (Equation 27) is increasingly dominated by the viscous term, as $\dot{D}$ accelerates. Neglecting the elastic term in Equation 27 yields:

$$\frac{\partial \Delta\sigma}{\partial D} = -\frac{3}{2} \frac{|f'(D)|}{f(D)} s_{ax}. \tag{45}$$

Using the equations for $f'(D)$ Equation 24 and $f(D)$ Equation 23, it can be seen that a low value of γ leads to a very steep $\frac{\partial \Delta\sigma}{\partial D}$. This likely explains the gentler stress drops shown in Figure 5h. We suspect that a large D_0 leads to a similar effect on $\frac{\partial \Delta\sigma}{\partial D}$ and accounts for the progressive stress drop in Figure 5f. It is noteworthy that our inversion for Westerly granite predicts a sharp stress drop, even though it relies on data that does not span the interacting crack regime ($D > D_c$, i.e., only pre-peak data is used in Figure 7a, and minimum creep strain rates in Figure 7b).

Our 2-D simulations help us assess how the change of crack growth regime affects the spatial pattern of damage as it transitions from distributed to localized (Figure 10c). In particular, the initial phase of distributed damage growth appears to coincide with the non-interacting regime. Damage increases uniformly, smoothing any pre-existing initial damage heterogeneity, and reaches a near constant value (~0.45) in the bulk rock when damage bands begin forming. We interpret this uniform value as related to D_c. Specifically, the distributed build-up of damage (snapshots 1, 2, and 3 in Figure 10c) proceeds in the non-interacting regime, in which damage is uniformly capped at ~D_c. Stress concentrations due to numerical noise or prescribed heterogeneities can however trigger the switch to the interacting regime in some portions of the sample (along the sides in snapshot 5 of Figure 10), leading to the localization of damage bands. Interestingly, the stable, uniform growth of damage when $D < D_c$ is probably the reason for the good agreement between our 2-D simulations and our 0-D models, which are by definition "homogeneous" (Figure 10a). The post-peak behavior predicted by the SCAM model is however significantly different in 2-D versus 0-D simulations. This is because it is driven by retro-actions between damage localization within a band and the stress field of the surrounding rock that cannot be captured in a pointwise model.

The distinct regimes of crack growth are also responsible for the two stages of creep observed in our constant stress simulations (Figures 4c and 4d, see Section 3), as well as in brittle creep experiments (Figure 1). In the representation of Figure 6a, a constant stress experiment simply maps as a horizontal line starting from any point of the constant strain rate trajectories prior to the peak stress. In order to break the material under constant stress, the K_I trajectory has to remain in the domain $K_I > 0$ up to $D = 1$. There thus exists a threshold in differential stress $\Delta\sigma_{bc}$ that must be met for the sample to fail macroscopically. Otherwise, the accumulation of damage under constant stress will decrease K_I all the way to negative values, inhibiting the growth of further damage. This threshold corresponds to the largest differential stress able to produce a stress concentration factor equal to zero. It is represented in Figure 6a by the summit of the dashed contour of $K_I = 0$, and corresponds to a value of around 720 MPa for a confining pressure of 150 MPa with our inverted Westerly granite parameters. Overall, $\Delta\sigma_{bc}$ can be thought of as a theoretical minimum strength of the rock, which is a function of confining pressure only (continuous blue line in Figure 11). If a brittle creep test is carried out under a constant differential stress above $\Delta\sigma_{bc}$, the damage state will eventually reach D_c in a finite amount of time, then transition to the interacting regime that allows failure. In this case, the creep test will begin by a decrease in K_I that manifests as a decrease in the macroscopic strain rate referred to as decelerating or primary creep (Figure 4c). We note that the minimum brittle
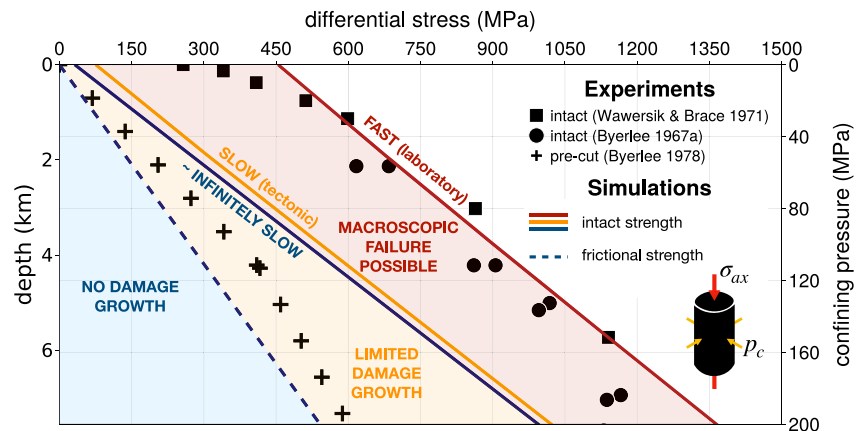
Figure 11. Brittle yield envelopes of the SCAM model calibrated against Westerly granite data (lines), compared to the experimentally determined strength of intact samples (Byerlee, 1967; Wawersik & Brace, 1971) (squares and circles) and pre-cut samples (Byerlee, 1978) (crosses). Red and orange plain lines correspond to peak strengths at $\dot{\varepsilon}_{ax} = -10^{-5}$ s^{-1} and -10^{-15} s^{-1}, respectively. The plain blue line corresponds to the minimum failure strength near the limit of infinitely slow strain rates. Modeled failure envelopes exhibit a constant effective friction coefficient of ~0.96 and strain rate-dependent cohesion. The dashed blue line represents the Mohr-Coulomb yield envelope associated with no cohesion and a friction coefficient $\mu = 0.7$, which corresponds to the friction used on shear defects and on macroscopic shear bands in the SCAM simulations.

creep strain rate should be captured accurately in 0-D simulations, since it corresponds to the strain rate at $D \sim D_c$, the extreme value of damage at which damage can grow in a distributed fashion. Finally, as the system switches to the interacting regime, K_I and the macroscopic strain rate both increase, first slowly then catastrophically, accounting for tertiary creep and failure of the sample. The idea that the transition to an accelerating regime of crack interaction up to failure corresponds to crossing a threshold in damage D_c explains the observations of Baud and Meredith (1997), who noted that the transition to tertiary brittle creep coincided with a critical extent of microcracking.

5.2. Revisiting the Byerlee Limit

Figure 11 shows failure envelopes for Westerly granite as determined with intact samples (peak stresses at laboratory strain rate, e.g., Byerlee (1967); Wawersik and Brace (1971), black circles and squares), as well as pre-cut samples (the "maximum friction" point from Byerlee (1978), black crosses). Both are on the order of hundreds of MPa, and increase linearly with confining pressures in the 20–200 MPa range. The intact envelope has a steeper slope and lies ~400−500 MPa above the pre-cut strength. Both our 0-D and 2-D models reproduce the intact envelope under the same laboratory strain rate of 10^{-5} s^{-1} (red line). The simulated envelopes are linear in confining pressure and display an effective cohesion of 94 MPa (inferred by linear regression of the red curve). On the other hand, the standard Mohr-Coulomb plasticity framework, with no cohesion and a friction coefficient of 0.7 provides a good fit to the strength of pre-cut samples (dashed blue line).

If one was to model the transition from intact to broken through strain-softened plasticity (Figure 2a), the friction should drop from ~0.96 to ~0.7, and the cohesion from 94 to 0 MPa. This should occur over a very small amount of plastic strain Δe_{II}^p to produce a sharp stress drop. It should be noted that a high "intact" friction coefficient, such as ~0.96, would produce unrealistic shear band orientations (e.g., Coulomb angles of ~23° between the band and σ_1). Within this model, friction is a property of the bulk material that must evolve as deformation accrues. By contrast, within the SCAM framework, friction is an intrinsic property of planar discontinuities in the rock that manifests at two scales. Friction first conditions slip on small-scale discontinuities (shear defects) whose interaction leads to the formation of larger-scale frictional interfaces (macroscopic shear bands). Those two frictional scales are characterized by the same friction coefficient and no cohesion. Until cracks coalesce, frictional sliding only occurs at the scale of shear defects, and its effect on the material is resolved through its induced stress concentration leading to tensile cracking. After coalescence, the broken material acts as a new frictional zone that generates its own stress perturbations on the surrounding "unbroken" material. It leads, in 2-D setups, to a shear band growing along a direction in which macroscopic stress concentrations amplify damage growth, yielding a

large differential stress drop of hundreds of MPas, which takes place over a very small range of axial strain (Figures 10a and 10b).

It is remarkable that our best fitting coefficient of friction for Westerly granite data (0.7)—which is constrained by data up to the peak strength—also fits the strength of pre-cut samples (dashed blue line in Figure 11). This supports our approach of switching from a damage model to cohesionless Mohr-Coulomb plasticity while retaining a constant coefficient of friction. This approach has the advantage of producing consistent shear band angles of around 30° to the most compressive stress (Figure 10c).

The SCAM framework also allows us to investigate failure at much slower deformation rates because brittle creep data contributes strong constraints on the rate dependence of the pre-peak behavior (Figures 5a and 10b), which is rooted in sub-critical crack growth. As an example, the 0-D failure envelope at a tectonic strain rate of 10^{-15} s^{-1} is shown by the orange line in Figure 11, and represents a constant strength contrast of ∼300 MPa relative to laboratory strain rates (red line). Compared to the laboratory strain rate simulations, the tectonic strain rate envelope amounts to lower effective cohesion (∼15 MPa) and a similar effective friction. To investigate the model's behavior in the limit of extremely slow strain rates, we construct an estimate of minimum intact strength using the 0-D SCAM model (solid blue line). We calculate it as the differential stress value at $D = D_c$ that would drive a damage growth rate arbitrarily set to 0.1 per billion year. This yields a line with an intercept that is still significantly greater than zero ($C \sim 6.4$ MPa). Overall, the effective cohesion of the brittle failure envelope can be thought of as a strain rate dependent term that does not entirely vanish in the limit of long loading times (e.g., planetary lifetime). The effective friction coefficient however remains invariant with respect to strain rate.

In summary, while standard strain-softened plasticity treats the brittle limit as an envelope that can move with accumulated plastic strain, the SCAM model treats it as a tenuous failure domain (red area in Figure 11) whose upper boundary depends on strain rate. Specifically, the maximum stress that must be attained for the rock to fail macroscopically can vary by ∼400 MPa between tectonic and laboratory conditions (10 orders of magnitude in strain rate). This effect is, by definition, not captured by rate-independent elasto-plastic models. On the other hand, the onset of damage growth is not sufficient to define the lower boundary of the failure domain. In order to activate inelastic strain, stresses must exceed a threshold that corresponds to $K_I(D_0) = 0$, that is, the activation of tensile cracking through frictional sliding on small defects. Because frictional sliding is indexed on meeting a cohesionless Mohr-Coulomb criterion with a friction of 0.7, this threshold is closely related to the dashed blue line in Figure 11. Exceeding this threshold however does not guarantee macroscopic failure. If differential stress remains between the dashed and solid blue lines (orange area in Figure 11), damage can be generated in the isolated crack regime, but will never reach D_c in a reasonable amount of time. The rock will thus never fail.

5.3. On the Meaning of the SCAM Micromechanical Parameters

Modeling progressive brittle failure with the SCAM model involves a number of parameters that lend themselves to micro-mechanical interpretations. However, the numerous simplifications made by the wing crack model (Ashby & Sammis, 1990), and the use of empirical rules for shear modulus weakening and sub-critical crack growth warrant some caution in doing so. Here we discuss the extent to which parameter values determined by calibrating SCAM against laboratory data provides meaningful information on a rock's microstructure.

Previous studies applying the wing crack micromechanical framework (Ashby & Sammis, 1990), such as Bhat et al. (2011) and Brantut et al. (2012), made the assumption that wing crack initiation happens at $K_I = K_{IC}$. In that case, the analytical expression for K_I (Equation 3 in Ashby and Hallam (1986)) can be used to constrain μ, a and K_{IC} given prior knowledge of a or K_{IC}, and of the axial stress of a sample at the onset of microcracking σ_{1c}, for various confining pressures. The onset of microcracking is typically indexed on the onset of dilatancy or acoustic emissions (Ashby & Sammis, 1990; Brace et al., 1966) (Figure 1). Applying this method to a linear fit of the Brace et al. (1966) data ($\sigma_{1c} = 3.6\sigma_3 + 100$ MPa) yields $\mu = 0.69$, $a = 0.58$ mm, assuming the fracture toughness $K_{IC} = 1.29$ MPa·m$^{1/2}$ determined by our joint inversions in Section 3.3. This coefficient of friction is very close to our estimate, but the crack radius is two orders of magnitude larger than our value of 6.66 μm, closer to the rock's grain size: the length scale considered susceptible to drive wing-cracking. For Darley Dale sandstone, X. Wu et al. (2000) used the same methodology and obtained $\mu = 0.69$ as well as $K_{IC} \leq 0.1$ MPa·m$^{1/2}$, assuming $a = 0.11$ mm. These values differ from our inversion results of $\mu = 0.51$, $K_{IC} = 1.4$ MPa · m$^{1/2}$ and $a = 0.65$ mm, especially for K_{IC}. These differences may be attributed to our use of a sub-critical crack growth law as opposed to

$K_I = K_{IC}$. We also note that because K_I scales as $\sqrt{a}$, our inversions do a better job at constraining a ratio of $K_{IC}/\sqrt{a}$ rather than K_I or a individually. Some trade-off is therefore expected between these values. It is noteworthy that the data against which the SCAM model parameters were inverted are much more complete than the data used in the studies discussed above. Specifically, our data includes stress-strain curves up to the peak stress (as opposed to a single point: the onset of dilatancy). We however acknowledge that at the peak stress, the discrepancy between the wing-crack model and the real rock microstructure may become large, introducing some bias in our parameter estimate.

Inspecting Figure 12 of Ashby and Sammis (1990) also reveals that wing-crack based damage mechanics can fit the very first portion of the experimental failure envelope of Westerly granite (i.e., at confining pressures between 0 and a few 100 s of MPas), but fail to predict peak stresses at greater pressures due to the non-linear dependence of intact rock strength with respect to confining pressure (visible in Figure 11: squares and circles). Ashby and Sammis (1990) suggested that the curvature of the experimental failure envelope of Westerly granite might result from low temperature ductile flow occurring within weak granite minerals. This hypothesis was tested by Bhat et al. (2011) by modeling a bi-mineralic quartz-feldspar assemblage with a dislocation glide flow law. It was found consistent with the experimental failure envelope at greater confining pressures. Broadly speaking, inverting experimental data over a large range of pressures using a model based only on fracture growth likely neglects processes that can significantly affect the mechanical response, such as intra-grain dislocation glide. This leads to inverted fracture parameters whose value can deviate from their expected range, since they are forced to explain behaviors caused by other deformation mechanisms. The exact value of the parameters should therefore not be over-interpreted. The value of the SCAM model lies more in its ability to extrapolate micromechanics-based rock behavior to larger scales, rather than in its informative power about rocks' intrinsic parameters.

6. Toward an Application to Tectonic Problems

In Section 3, we introduced and calibrated the 0-D SCAM micro-mechanical model against experimental data to capture the mechanical behaviors of Westerly granite and Darley Dale sandstone in the brittle regime. Section 4 was dedicated to the implementation of this model in a 2-D plane strain tectonic solver to investigate the behavior of the calibrated model when strain localization is made possible. We validated the model by showing that it still accurately predicts experimental data in 2-D. Next, we turn to the end-goal of the SCAM framework by showcasing initial attempts at using it to model tectonic deformation.

6.1. Crustal-Scale Numerical Setup

As a first step toward using the SCAM model for long-term tectonic problems, we focus on the initial stages of faulting of a 10-km thick brittle plate overlying a 40-km wide and 10-km thick low-viscosity Newtonian medium subjected to gravity (9.8 m s^{-2}) and to a constant horizontal extension rate (Figure 12). An additional upper layer of low-viscosity "sticky air" ensures the brittle plate has a traction-free top boundary (Gerya, 2010). The plate is notched at the center of its lower edge by a 1 km long and 0.75 km thick protrusion of the underlying viscous layer to promote strain localization in the middle of the domain. The latter is discretized using a cell size of 100×250 m within 8 km of the top and bottom walls, and an greater resolution, with a cell size of 100×100 m in the remainder of the domain containing the brittle plate. The plate and the fluid layer underneath it are assigned a density of 2,700 kg m^{-3}, while the uppermost fluid layer's density is 0.01 kg m^{-3}, to ensure negligible pressures at the top of the plate. The left and right sides are prescribed a fixed outward horizontal velocity amounting to a constant extension rate of 10 cm/yr (strain rate of $\sim 10^{-13}$ s^{-1}). The velocities of the top and bottom boundaries are set to satisfy volume conservation within the domain and to preserve the height of the brittle plate's top surface. All boundaries are free slip. As in simulated experiments, the maximum viscosity η_{max} allowed in the domain is chosen such that its Maxwell time (η/G) is 50 times longer than the longest simulation time. This guarantees that the brittle plate—whose viscosity is set to η_{max}—retains an elastic response throughout the entire simulation. The exact value of η_{max} will therefore not matter as long as it is large enough. To avoid large, computationally challenging viscosity contrasts within the model domain, the lower bound on viscosity is set to six orders of magnitude below the brittle plate's viscosity, and is assigned to the air and viscous lower layer. This guarantees that they behave as low-viscosity fluids during each simulation. This setup resembles that used by Lavier et al. (2000) and Olive et al. (2016) to investigate the effect of brittle strain softening and elasticity on extensional tectonic styles, within the standard elasto-plastic framework. One notable difference is that here the base of the
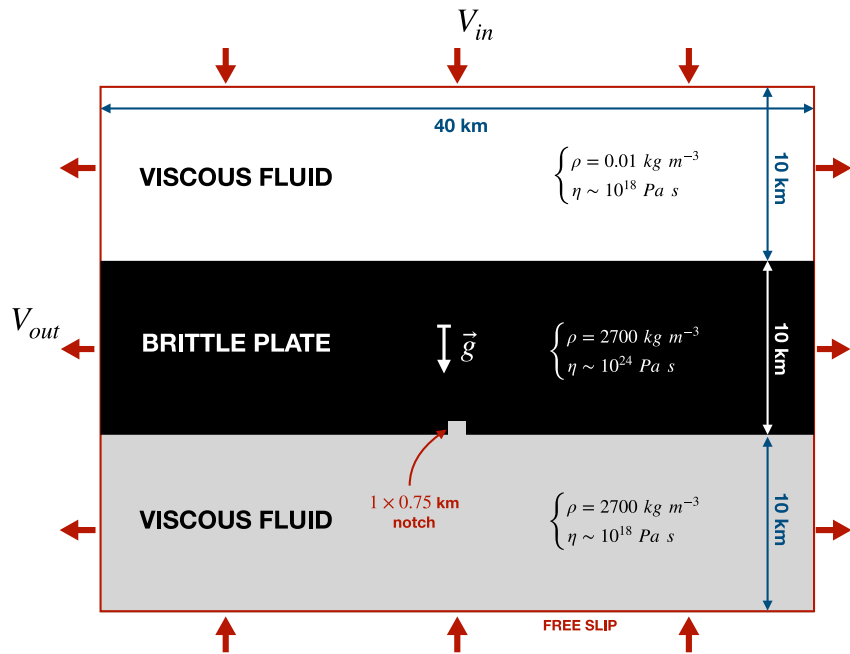
Figure 12. Numerical setup used to simulate the stretching of a rigid crustal unit in 2-D plane strain. The domain is 40 km long and 30 km thick and contains two 10-km thick low-viscosity layers at the top and bottom of a brittle plate of the same thickness. The brittle plate is notched by a 1×0.75 km protrusion of the underlying viscous fluid. Constant outward velocities at the left and right boundaries apply a constant stretching rate on the brittle plate, while the top and bottom boundaries are also assigned constant inward velocities to satisfy volume conservation. All boundaries are free of shear tractions.

brittle plate is a lithological boundary that gets advected as the plate thins (unlike, e.g., a thermal boundary that may experience diffusion).

We run two suites of simulations, one with the SCAM parameterization of brittle failure in Westerly granite (Table 1), and one with the standard strain weakened elasto-plastic (EP) approach, similar to the runs of Olive et al. (2016). Tectonic simulations using the SCAM model, like those presented in Section 4, include a switch to standard elasto-plasticity in fully damaged areas. Specifically, the damage viscosity is set to smoothly transition to a plastic viscosity as η_D approaches η_p over a viscosity range of $|\eta_D - \eta_p|$ equal to $\eta_{min}/50$. The locally broken material (i.e., $D = 1$) behaves as a Mohr-Coulomb plastic solid, with no cohesion and the same friction coefficient as that of the shear defects.

Standard elasto-plastic simulations, on the other hand, are parameterized to match the intact strength of the SCAM model calibrated on Westerly granite (Figure 11) under a laboratory strain rate ($10^{-5}\,\mathrm{s}^{-1}$, red curve) and under a tectonic strain rate ($10^{-15}\,\mathrm{s}^{-1}$, orange curve). These envelopes correspond to a similar friction coefficient $\mu = 0.96$ and cohesions C of 94 and 15 MPa, respectively (see Section 5.2). For concision, these simulations will be referred to as *EP-lab* and *EP-tecto*. In both cases the frictional parameters are linearly weakened over a critical amount of accumulated plastic strain $\Delta\varepsilon^p_{II} = 0.1$ down to $\mu = 0.7$ and $C = 0$ MPa, the frictional properties of the shear defects.

6.2. Development of Fault Networks

We first compare the faulting patterns produced by an elasto-plastic rheology (EP-tecto) versus the SCAM rheology during early rifting (up to $\sim$180 m of total extension). Figure 13 shows successive snapshots of accumulated plastic strain e^p_{II} (a1 to a3), second invariant of strain rate $\dot{e}_{II}$ (b1 to b3), and viscosity (c1 to c3), as extension of the EP-tecto plate progresses. Plastic yielding starts from the surface of the plate, where pressure, and therefore yield stress, is lowest. It progressively deepens as the yield criterion is met deeper and deeper due to elastic loading of the plate (Panels a1 and a2). Plastic yielding initially mostly develops in a distributed fashion
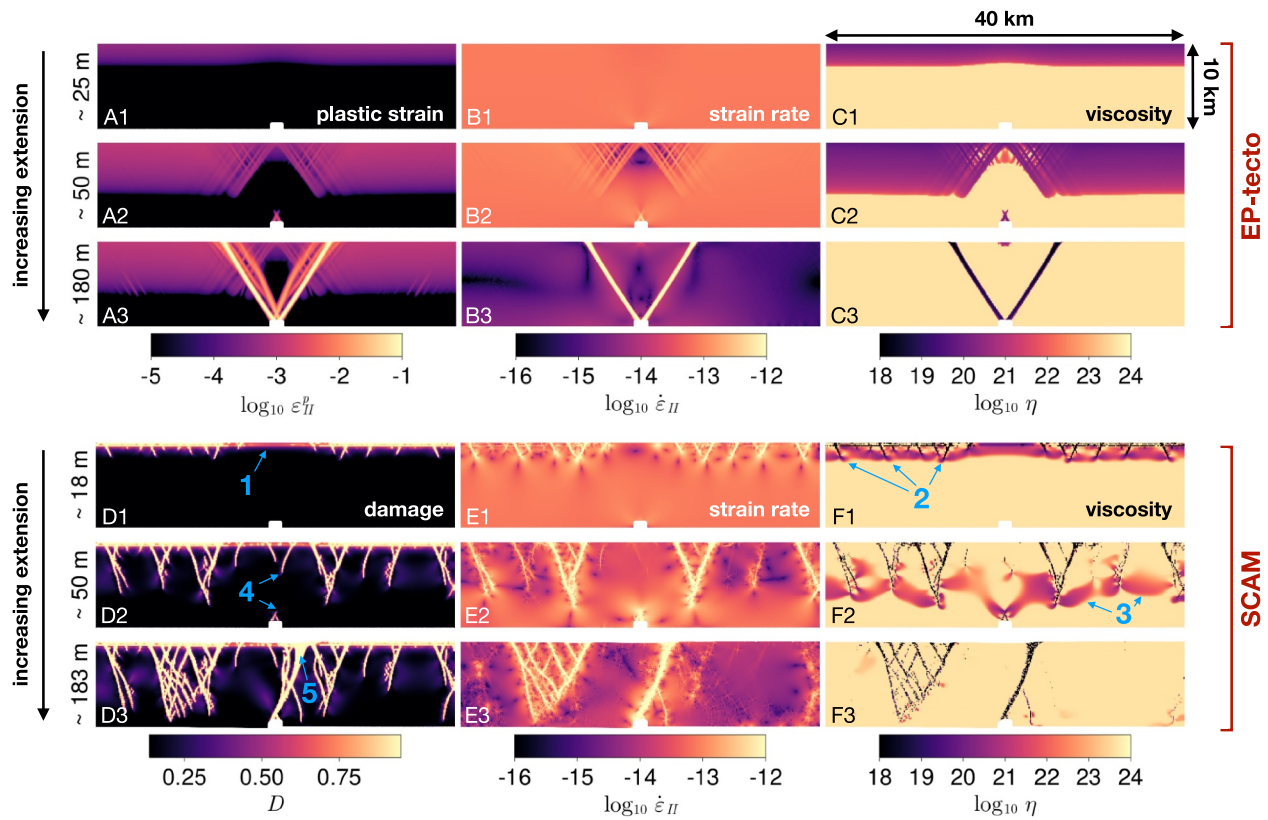
Figure 13. Snapshots of an early rifting simulation (10 cm/yr) in a 10-km thick brittle plate using the elasto-plastic EP-tecto parameterization (a–c) versus the SCAM model (d–f). Each row corresponds to a specific time (i.e., amount of finite extension) in the simulation. The first column shows the accumulated plastic strain for EP-tecto, and the damage field for the SCAM model. The second column shows the second invariant of the deviatoric strain rate tensor, and the third column displays the viscosity field within the brittle plate.

(second row), with plastic strain localization occurring once almost half of the plate has reached yielding. The zone of distributed yielding closer to the viscous protrusion, then transforms into an area densely populated with shear bands, of dip angle near 55°, each accommodating a very small fraction of the total extension rate (second row). Stress concentrations around the basal notch eventually lead to the formation of a pair of shear bands symmetrically cutting across the brittle plate, following the path of pre-existing superficial shear bands. Plastic strain accordingly localizes along two major antithetic shear bands (third row). The formation of these faults relax the elastic stresses within the plate and inhibit plastic yielding in the remainder of the plate (Panels b3 and c3).

The same setup using the SCAM flow law (Figures 13d–13f) shows a different story. Damage first increases uniformly within ~1 km below the surface of the brittle plate (Panel d1, blue arrow 1). After shallow damage exceeds values of 0.4–0.5 ($\sim D_c$), damage localization proceeds through the downward propagation of damage bands which promptly turn into plastic shear bands (first row). This occurs when the isolated crack regime transitions to the interacting cracks regime (see Section 5.1.2). The thickness of the shallow distributed damage zone (~1 km) is set by a competition between damage growth being activated deeper and deeper as K_I turns positive with loading, and the unstable growth of damage bands (which soon turns plastic) once D exceeds D_c. Damage banding unloads the surrounding material by releasing elastic stress through inelastic flow. The growth of these shear bands is self-promoted as the result of stress concentrations at their lower tips, which locally accelerate crack growth and coalescence. This dynamic is clearly visible on the viscosity snapshots, for example, Panel F1, where each fault has its own associated lobe of low viscosity (blue arrow 2), driven by damage growth. These lobes are accompanied by a front of low (damage) viscosity which deepens through time (Panel f2, blue arrow 3). This reflects the fact that with continued far-field loading, the depth at which K_I turns positive increases.

Growing faults tend to shield each other and alter the stress field in their vicinity, which leads to the development of complex networks shaped in a tree-like fashion (e.g., the imbricated fault structure that forms on the left side of

the plate in Panels d3–f3). After about 50 m of stretching, the concentration of tensile stresses around the viscous protrusion promotes the growth of a major fault, which first grows upward with a downward convex shape (Figures 13d2–13f2), connecting with one of the deepening faults (Panel d2, blue arrow 4), before a more favorably oriented branch eventually grows and bypasses the less favorably oriented pre-existing segment of the fault. This master-fault's dip angle increases from ∼60° at the bottom of the plate, to almost 90° close to the surface. As extension progresses, the uppermost part of the fault (Panel d3, blue arrow 5) rotates toward gentler dips, which progressively widens the thickness of the damage band near the surface, as shown in the last row of snapshots (blue arrow 5 in Panel D3). The dip angle of secondary faults is variable and ranges from 60° to 75° with segments locally close to vertical, reflecting the spatially variable distribution of stresses induced by the complex array of faults.

The fault angles with respect to σ_1 (here vertical) are overall smaller in the SCAM tectonic simulations (15–30°) than what was observed in our 2-D simulations of triaxial experiments (∼30°, see Section 4.4). These faults are closer to the Coulomb angle (23°) associated with the effective intact strength coefficient of internal friction of Westerly Granite ($\mu = 0.96$), than with the coefficient of friction at the micro-crack scale ($\mu = 0.7$). Some deviation from the theoretical value likely stems from heterogeneities in the stress field that develop through stress concentrations and complex interactions between growing shear bands. In simulation EP-tecto, the master fault orientations of around 33°, correspond to the Arthur angle $\theta_A = 45° - (\phi + \psi)/4$ (Arthur & Dunstan, 1977) associated with the prescribed initial internal friction coefficient of 0.96 without any plastic dilatancy ($\psi = 0$), which is a typical shear band angle found (along with the Coulomb angle) in numerical elasto-plastic simulations (Kaus, 2010).

Contrary to the EP-tecto simulation, the initiation of a fault cutting across the plate does not inhibit the activity on secondary faults, which continue to accommodate a significant amount of extension in the SCAM run (Figure 13, Panel b3 vs. e3). We note that EP simulations can produce such behavior, but it generally requires a small strength contrast between the fault zone and surrounding lithosphere (Lavier et al., 2000). To further characterize the partitioning of strain in the SCAM runs, Figure 14a represents the distribution of slip rates on the population of faults, sampled at different depths in the plate after ∼180 m of extension (Figures 13a3–13c3 and 13d3–13f3). We identify normal faults by locating positive peaks along a profile of horizontal strain rate $\dot{e}_{xx}$ along a line of constant depth. To mitigate resolution issues when two neighboring peaks are found, we only retain the larger of any two peaks distant by less than four cell sizes. We focus on peaks where strain rate exceeds $4 \cdot 10^{-13}$ s^{-1}, which
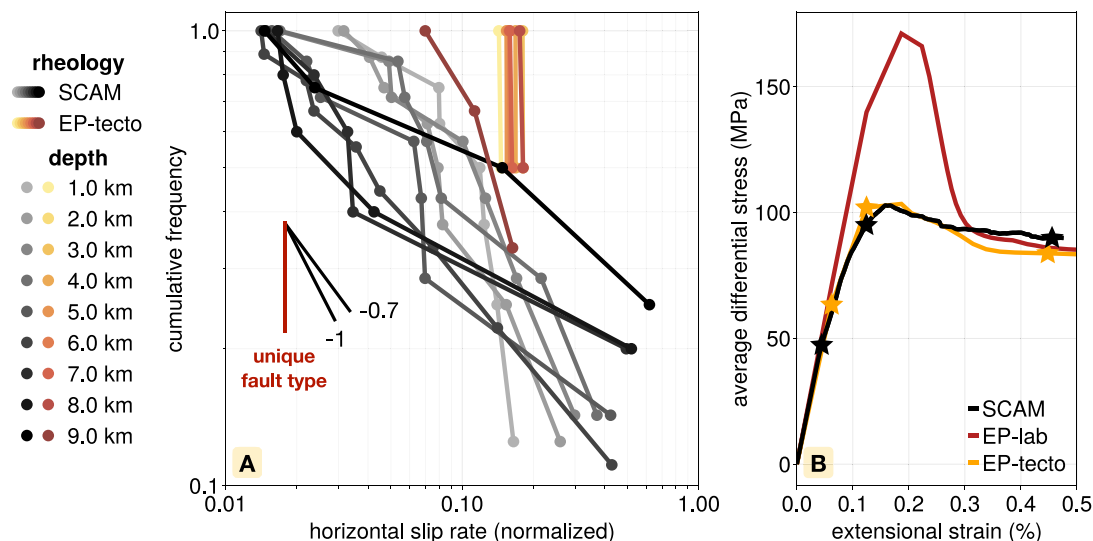

Figure 14. (a) Distribution of slip rates on fault populations sampled along different depths in a SCAM-based simulation (gray lines) versus simulation EP-tecto (yellow-to-red lines). Faults are measured after 180 m of total stretching, corresponding to Panels a3–c3 and d3–f3 of Figure 13. (b) Differential stress averaged across a 1 km-wide vertical band along the left side of the extended brittle plate, plotted as a function of total extensional strain. The black curve corresponds to the SCAM simulation, whereas the red and orange curves are associated to elasto-plastic simulations parameterized with short (EP-lab) and long-term (EP-tecto) intact strengths. Stars mark the timing of the snapshots displayed in Figure 13.

amounts to five times the background horizontal strain rate imposed by boundary conditions. The slip rate on each fault is then calculated assuming that the thickness of the faults is one cell length (100 m in these simulations).

Lastly, we find that the slip rates of the incipient fault population produced by the SCAM model follows a power law distribution of exponent close to 1 (gray lines in Figure 14a). This distribution likely originates in the tree-like, near-fractal nature of the fault network that emerges within the brittle plate. Simulation EP-tecto, on the other hand, rapidly produces two dominant faults with very similar slip rates, and virtually no smaller fault with slower slip rates. The distribution of fault slip rates produced by the SCAM run evokes the power law distributions exhibited by natural populations of normal faults. For example, the lengths and offsets of Basin and Range normal faults have been shown to follow a power law distribution with exponent close to unity (e.g., Marrett et al., 1999; Scholz et al., 1993). Natural rift systems are also known to partition extension onto multiple faults of varying sizes, such that all minor intrabasinal faults typically accommodate as much strain as a single half-graben border fault (Morley, 1996). Standard elasto-plastic models tend to localize deformation onto a small number of lithosphere-scale faults (Olive et al., 2016), but can also produce a wide range of fault sizes in the early stages of rifting, provided sufficient resolution is used (Naliboff et al., 2020; Pan et al., 2022). In this case, the distribution of fault sizes and offsets appears to depend on the amount and rate of strain softening, as well as on the overall extension rate (Naliboff et al., 2020). The SCAM model provides a novel framework to further explore this dependence without resorting to ad-hoc softening rules.

6.3. Strength of the Brittle Lithosphere

Figure 14b shows the differential stress averaged along the left side of the model domain throughout our early rifting simulations. All show an initial elastic increase, followed by a peak and a softening phase. The average peak stress reached in the SCAM simulation is ∼100 MPa. The softening phase is much less acute than in our simulations of triaxial experiments (Figure 10). This possibly reflects the progressive nature of the development of the fault network (Figure 13). The peak stress roughly coincides with the moment when a fault first connects the top to the bottom of the plate, shortly after snapshots D2–F2 in Figure 13. The steady, long-term stress (∼90 MPa in Figure 14b) is attained when one of the throughcutting faults has clearly developed into the dominant one accommodating the largest extension rate (Figure 13e3).

On the other hand, simulation EP-lab illustrates what happens when one models rifting with strain-softened elasto-plasticity calibrated on experiments conducted at laboratory strain rates (Figure 11). The plate reaches a significantly greater peak stress of ∼160 MPa (Figure 14b), and experiences more drastic weakening down to its long-term frictional strength, which is inferred from pre-cut samples ($\mu = 0.7$ and no cohesion). By contrast, simulation EP-tecto, which is calibrated to reproduce the intact strength of samples predicted by the SCAM model at tectonic strain rates (yellow line in Figure 11), unsurprisingly produces a stress-strain curve similar to the SCAM simulation (Figure 14b).

Through its built-in dependence on strain rate, the SCAM rheology can extrapolate crustal strength under tectonic conditions, even though it is entirely calibrated on laboratory data. It thus constitutes a promising alternative to the standard approach in tectonic modeling, which consists of using "Byerlee's law," that is, assigning the pre-cut sample strength to intact brittle lithosphere ((Brace & Kohlstedt, 1980)). The SCAM flow law has the advantage of using a single value of friction and a handful of micro-mechanical parameters to predict the lithosphere's intact strength across 10 orders of magnitude of strain rate. It self-consistently handles the transition from intact to broken (pre-cut), and does not require any empirical assumption on weakening strain. Alternatively, SCAM can be used to prescribe an intact strength that is appropriate at tectonic strain rates, for use in standard elasto-plastic models (e.g., simulation EP-tecto). This approach, however, does not solve the problem of the ad-hoc weakening strain.

6.4. Growth of Geological Structures

In order to compare the tectonic structures formed after greater amounts of finite extension by the SCAM and elasto-plastic (EP-tecto) rheologies, we performed three additional simulations under strain rates of 1, 1, and 10 mm/yr for each rheology. Due to the computationally demanding nature of the SCAM model, we decreased the resolution of the spatial domain using a cell size of 250×500 m within 8 km of the top and bottom walls, and a greater resolution, with a cell size of 250×250 m in the rest of the domain containing the brittle plate.

Snapshots of the second invariant of strain rate $\left(\dot{e}_{II}\right)$ fields at different times are displayed in Figure 15. The first three rows correspond to successive times throughout the SCAM simulations after ∼251, ∼1,079, and ∼3,457 m of horizontal stretching, respectively. The fourth row corresponds to snapshots of elasto-plastic simulations performed under the same extension rates, after ∼3,457 m of extension. The elasto-plastic simulations remain unsurprinsingly insensitive to a change of strain rate (e.g., Olive et al., 2016), as they all develop the same central graben structure (Figures 15d–15f).

The SCAM simulations, on the other hand, generate features that vary with extension rate. The first one is the location of the cluster of faults in the hanging-wall ((Figure 15a1–15c1). The faster the extension rate, the closer this cluster of secondary faults lies to the master fault, with distances ranging from 15 to 7 km. The second feature is the geometry of the rift after 3,457 of extension (Panels a3–c3). The rift structure shows a greater degree of asymmetry with increasing extension rate. This is particularly well expressed in topography, which corresponds to a symmetric graben in Panel a3 but is closer to a half-graben in Panels b3 and c3, as more extension is accommodated of the central right-dipping fault. We acknowledge that some of this variability could be attributed to stochasticity in marker positions, coupled with strong non-linearities of the SCAM flow law. We however ran the SCAM simulations a second time using different randomly assigned marker positions, and otherwise identical parameters. This second set yielded the same pattern of strain rate dependence as illustrated in Panels a3–c3.

Extension rate is known to influence rifting styles, primarily by modulating the thermal structure (Buck, 1991; Lavier & Buck, 2002). Our results suggest that it may play an additional, more subtle role by modulating the very processes of fault development. Specifically, the SCAM model introduces a strain rate dependence of brittle deformation by transiently activating a moderate to low viscosity in portions of the upper crust where damage is actively growing (e.g., Panels f1 and f2 of Figure 13). An analogous strain rate dependence of deformation was previously noted by Olive et al. (2016) in rifting simulations that treat the upper crust as a visco-plastic medium rather than an elasto-plastic medium. In the present case, however, the viscosity of the upper crust has a physical meaning (η_D, related to the damage growth rate), as opposed to an arbitrarily high value meant to simulate a stiff visco-plastic upper crust.
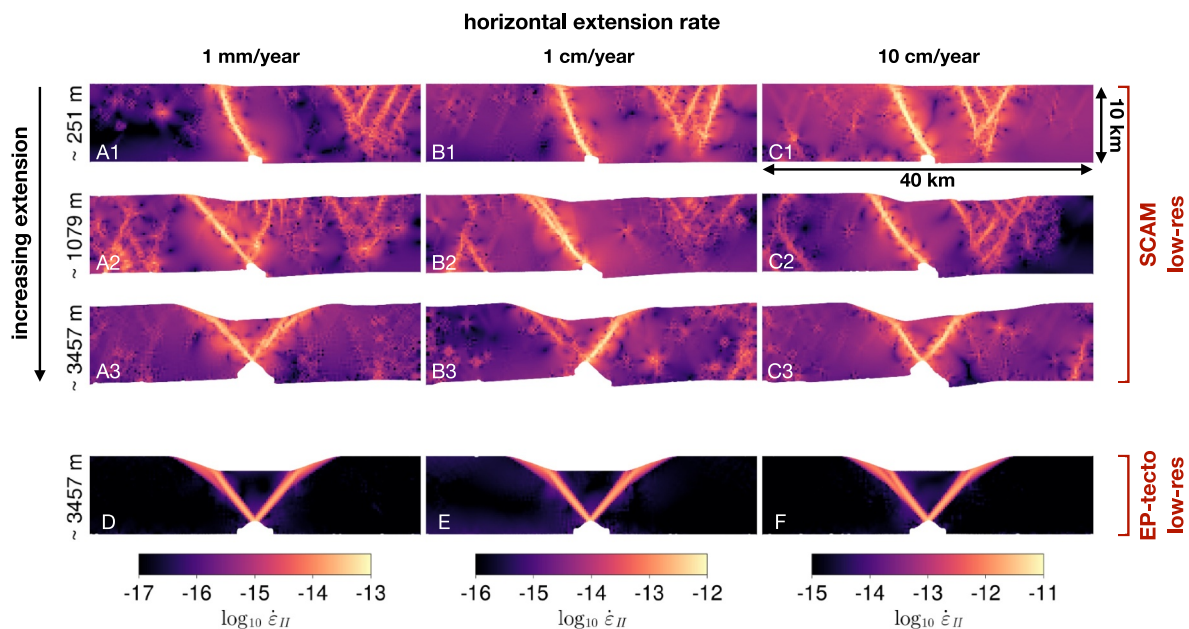
Figure 15. Numerical simulation of about 3.5 km of extension of a 10-km thick brittle plate, at varying rates (columns). Snapshots of the second invariant of strain rate at different amounts of finite extension (shown on the left), for a brittle plate governed by a–c the SCAM flow law, and d–f the EP-tecto rheology. The model resolution has been reduced compared to Figure 13 to reach greater amounts of finite extension in reasonable time.

6.5. Upscaling the SCAM Parameters

The results presented thus far show that a flow law indexed on the activity of sub-millimetric rock defects, and calibrated on decimeter-sized samples can produce reasonable deformation patterns when applied to tectonic problems at scales >10 km. This fact does not negate the implication of larger defects (>10 cm) in the nucleation of crustal faults, but highlights that they need not be explicitly described in our constitutive relation. These intermediate-scale defects can be thought of as emerging through the formation of distributed damage bands, albeit only at scales greater than the numerical grid size, before dominant crustal-scale bands fully develop (e.g., Figure 13d1–13f1). In other words, the coalescence of sub-millimetric shear cracks produce diffuse proto-faults, and stress concentrations at their tips generate further localization at larger and larger scales.

Nonetheless, it is legitimate to wonder how differently our model would behave if it was based on larger (e.g., metric) shear defects. To address this question, we assess the effect of initial defect size a on the two extreme measures of rock strength in the SCAM framework: the minimum strength that characterizes extremely slow deformation, and the maximum strength at very high strain rates. The absolute lower bound on SCAM strength is given by the maximum differential stress satisfying $K_I = 0$ (Figure 6, end of Section 5.1.2). It corresponds to the differential stress that must be reached for macroscopic failure to be achievable, albeit after an infinitely long time (plain blue line in Figure 11). The expression of K_I (19) is a function of σ_1, σ_3, μ, a, and N_v (through D_0), but in the special case where $K_I = 0$, the explicit dependence on a drops, such that the maximum differential stress at $K_I = 0$ only depends on σ_3, D_0 and μ. Assuming μ is constant across scales, we end up with a lower bound on strength that only depends on $D_0 = \mathrm{f}(a, N_v)$.

Interestingly, this property can be used to constrain a plausible range of D_0 values to be used in tectonic simulations. The minimum strength (continuous blue line in Figure 11) must exceed the stress required to slip on a favorably oriented pre-existing frictional surfaces (e.g., ~500 MPa for $\sigma_3 = 150$ MPa, the value used to construct Figure 6; dashed blue line in Figure 11). The minimum strength must also be lower than the strength measured in the laboratory at the slowest possible strain rate (somewhere within the red area in Figure 11). Taking 90% of the peak value from Wawersik and Brace (1971) (e.g., 1,150 MPa for $\sigma_3 = 150$ MPa) as a rather conservative estimate, considering that Brantut et al. (2012) observed brittle creep failure at ~77% of estimated peak strength under 50 MPa of confining pressure, brackets the minimum strength for $\sigma_3 = 150$ MPa between ~500 and ~1,150 MPa. This corresponds to a range of D_0 between 0.06 and 0.4.

On the other hand, the maximum strength of the material at very fast strain rates can be assessed by equating Equation 19 to K_{IC}, and rewriting it as a function of σ_1. This gives an equation whose maximum with respect to D yields the maximum differential stress a rock can withstand (Figure 6), as cracks grow critically at seismic wave speeds (Bhat et al., 2012). This maximum stress roughly scales as $K_{IC}/\sqrt{a}$. It follows that the difference between the maximum differential stress at $K_I = K_{IC}$ and at $K_I = 0$, a measure of the overall strain rate dependence of the SCAM model, approximately scales as $a^{-1/2}$. If fracture toughness is a scale-invariant, intrinsic property of the material, increasing the size of the initial shear cracks brings the maximum and minimum strengths closer and closer to each other, severely suppressing the strain-rate dependence of the material's intact strength. This result is a fundamental property of the wing-crack model of Ashby and Sammis (1990), and does not depend on the specifics of the SCAM model. Whether it applies to natural systems remains an open question, as it is well known that fracture toughness can vary significantly across scales.

7. Conclusions and Perspectives

In this paper, we introduced a Sub-Critically Altered Maxwell (SCAM) framework to describe brittle deformation in long-term tectonic models. It is a set of constitutive equations that capture experimentally described behaviors of rocks at upper crustal pressures and temperatures. It is based on the evolution of an internal damage state and on its interactions with the elastic properties of the material. The model also allows large deformations by branching to plastic behavior after microcracks interact and coalesce. The SCAM model has several notable properties that make it a promising alternative to standard elasto-plastic models, or a way to improve their parameterizations of brittle yielding. Elastic properties are permanently altered due to their indexation on damage. Damage growth is a time-dependent process that is activated at stresses far below failure strength, through frictional sliding on shear defects distributed throughout the rock. It promotes strain softening pre-peak and self-consistently generates the successive stages of brittle creep. Creep behavior results from the transition from negative to positive retro-action

between damage and damage growth, which represents increasing interactions between lengthening cracks. The SCAM model also produces two yield strength using a single friction coefficient and no cohesion: a peak failure strength with high effective friction and strain rate dependent cohesion, which ultimately transitions to a rate-independent residual strength that obeys Byerlee's law. Despite the high effective friction (∼1), shear band orientations in 2-D plane strain simulations remain consistent with the true friction coefficient that describes the strength of shear defects ($\mu \sim 0.7$). The SCAM model can be calibrated against experimental data using prior knowledge on well-constrained rock properties to model the deformation of a specific lithology. Here Bayesian inversions of experimental data on Westerly granite and Darley Dale sandstone led to a set of reasonable micromechanical parameters whose impact on the macroscopic behavior of the rock can be straightforwardly interpreted.

Preliminary results of rifting simulations in a 10-km thick brittle plate subjected to gravity show that the SCAM model generates a population of faults with power-law distributed slip rates, akin to the distribution of natural fracture sizes and fault offsets, and likely introduces a strain rate dependence of the geological structures that develop at large strains. These features make it a good candidate to further investigate the complexity of brittle behavior across scales.

In designing the SCAM framework, we have strived to capture key micromechanical processes while keeping the model as simple as possible. This came at the cost of a few simplifications that may be relaxed in future work. A first strong assumption is that weakening of the shear modulus occurs isotropically, even though the orientation of the shear defects is strongly anisotropic. This assumption has the advantage of reducing the complexity of the constitutive law and simplifying its interpretation, but lacks consistency when relating crack geometry to macroscopic behavior. Within this assumption, however, a more consistent approach to damage-induced elastic weakening could be to assume isotropic weakening in the plane containing the crack normals (the (σ_1, σ_3) plane), and no weakening in the perpendicular direction. Such anisotropy however implies that the 2-D plane strain condition can no longer be satisfied for arbitrary extremum stresses, that is, enforcing $\varepsilon_2 = 0$ could lead to σ_2 not being an intermediate stress between σ_1 and σ_3.

In addition to neglecting material anisotropy, the evaluation of K_I (Section 2.3) assumes that all cracks remain oriented at 45° with respect to σ_1 regardless of the stress and material rotations that may occur during large deformations. This assumption can lead to significant errors on the stresses resolved on shear defects. We note that the strains associated with shear band localization are on the order of a few percent, and thus should not be accompanied by significant finite rotation. On the other hand, large strains could conceivably rotate shear defects out of an optimal orientation in a long-term tectonic simulation. From a theoretical and computational point of view, keeping track of multiple shear defect orientations in an evolving stress state is challenging, in part because evaluating stress intensity factors and interaction terms would become very complex. The very definition of damage should also be revised to account for curving wing-cracks that grow along a changing σ_1 direction, and/or different sets of tensile wings associated with different sets of shear defects.

Another possible improvement for long-term tectonic modeling would be to allow damage to partially or completely heal over long time scales. This would promote the progressive recovery of intact elastic properties within abandoned shear bands, and require a re-mobilization of micro-scale frictional processes in order to re-activate a de-activated fault. To this end, a sub-critical crack growth law similar to that of Darot and Gueguen (1986) seems adequate. Crack growth is formulated as a thermally activated process where the growth or healing of a crack is indexed on the sign of the energy balance associated to the incremental advance of the crack front. This formulation has a more robust thermodynamical foundation than Charles' (1958) law and also accounts for the effect of temperature. It however involves more parameters, which is why we restricted ourselves to a simpler version of Charles' law in this work.

Finally, and importantly, the present study neglected the intrinsically dilatant effect of mode-I crack growth. Incompressibility is a common simplification in long-term tectonic models (Gerya, 2010), which amounts to setting the Poisson's ratio to 0.5 and the dilatancy angle to zero when modeling brittle failure with Mohr-Coulomb plasticity. Recent studies have shown that accounting for elastic and plastic compressibility noticeably impacts the outcome of tectonic simulations. Specifically, Duretz et al. (2021) found that compressibility hinders strain localization (it produces broader shear zones), and can facilitate the convergence of numerical solvers. A mechanically consistent way of introducing inelastic dilatancy within the elastically incompressible ($\nu = 0.5$) SCAM model would be to use the constitutive law developed by Bhat et al. (2012). Their approach consisted of assessing

the Gibbs free energy of a damaged solid (assuming the (Ashby & Sammis, 1990) micro-mechanical model), and deriving it with respect to stress to yield effective elastic compliances. This approach outlines two sources of volumetric strain during damage accumulation: one directly results from the elastic compressibility of the material, which is altered by damage, the other represents a coupling between shear and volumetric deformation (a direct consequence of mode-I cracks being wedged open by shear defects). An elastically incompressible, yet inelastically dilatant SCAM model could focus on capturing this shear-volumetric coupling through an effective dilatancy angle that can be directly related to damage and stress Bhat et al. (2012). Dilatancy should cease as soon as cracks coalesce ($D \sim 1$), and give way to standard incompressible Mohr-Coulomb plasticity.

In its current state, the SCAM framework already unveils novel prospects for tectonic modelers. Keeping track of a damage field enables new connections between crustal scale simulations and key observables. Damage fields could straightforwardly be converted to seismic velocity maps for comparison with crustal tomography data. The distribution of damage along the model's free surface could also be used as a proxy for the erodibility of rocks exposed to weathering, and help understand variability in erosion rates across tectonically active landscapes (Gallen et al., 2015; Molnar et al., 2007) Finally, damage accumulation is intrinsically linked to an increase in porosity within the rock, and fracture connectivity is a primary control on fluid pathways. The evolving damage field could therefore be used as a proxy for the permeability of the brittle crust (e.g., Perol and Bhat (2016)) enabling coupled models of progressive brittle failure and fluid flow. This would enable the consideration of both poro-elastic feedbacks between fluid pressure and deformation, as well as alterations of mechanical properties through fluid-rock reactions.

Appendix A: Bayesian Inversion Procedure

A1. Mathematical Description

As illustrated in Section 3, our "forward" problem consists of predicting a vector of data points $\mathbf{d}$, for example, a time series of stress or brittle creep strain rates, given a set of rock parameters (Table 1) stored in a vector $\mathbf{m}$. This problem synthetically writes $\mathbf{d} = \mathbf{g(m)}$. By contrast, the inverse problem consists of finding the distribution of model parameters that best fits known experimental data $\mathbf{d_{obs}}$ with associated uncertainty. We adopt a least-squares approach in which all probability distributions quantifying uncertainties are Gaussian. Uncorrelated data uncertainty can thus be represented as a Gaussian distribution centered on $\mathbf{d_{obs}}$ with a diagonal covariance matrix $\mathbf{C}_d$. Similarly, a-priori knowledge on the distribution of model parameters can be assumed to follow a Gaussian distribution centered on $\mathbf{m}_{prior}$, with diagonal covariance matrix $\mathbf{C}_m$.

We seek the best-fitting model $(\widetilde{\mathbf{m}})$ which minimizes the log-likelihood function: a measure of distance between $\mathbf{d_{obs}}$ and $\mathbf{d}$, weighted by data uncertainty and prior knowledge:

$$S(\mathbf{m}) = \left(\mathbf{g(m)} - \mathbf{d_{obs}}\right)^T \mathbf{C}_d^{-1}\left(\mathbf{g(m)} - \mathbf{d_{obs}}\right) + (\mathbf{m} - \mathbf{m_{prior}})^T \mathbf{C}_m^{-1}(\mathbf{m} - \mathbf{m_{prior}}). \tag{A1}$$

The log-likelihood is then minimized using a Gauss-Newton iterative algorithm (Tarantola, 2005). The iterative scheme, initialized at $\mathbf{m_0} = \mathbf{m_{prior}}$, reads:

$$\mathbf{m_{n+1}} = \mathbf{m_n} - \kappa_n\left(\mathbf{G}_n^t \mathbf{C}_D^{-1} \mathbf{G}_n + \mathbf{C}_m^{-1}\right)^{-1}\left(\mathbf{G}_n^t \mathbf{C}_D^{-1}\left(\mathbf{g(m_n)} - \mathbf{d_{obs}}\right) + \mathbf{C}_M^{-1}(\mathbf{m_n} - \mathbf{m}_{prior})\right), \tag{A2}$$

where n and $n + 1$ refer to the current and next iteration, $\kappa_n \leq 1$ is the step multiplier, a hyperparameter that can be tuned to help convergence in case of strong non-linearities in the log-likelihood function. $\mathbf{G}$ is the Jacobian matrix:

$$G_n^{ij} = \left(\frac{\partial g_i}{\partial m_j}\right)_{\mathbf{m_n}}. \tag{A3}$$

The posterior model covariance matrix, a measure of the uncertainty on the inverted parameters, is then computed as

$$\widetilde{\mathbf{C}}_{\mathrm{M}} \simeq \left(\mathbf{G}^{t}\mathbf{C}_{\mathrm{D}}^{-1}\mathbf{G} + \mathbf{C}_{\mathrm{M}}^{-1}\right)^{-1} = \mathbf{C}_{\mathrm{M}} - \mathbf{C}_{\mathrm{M}}\mathbf{G}^{t}\left(\mathbf{G}\mathbf{C}_{\mathrm{M}}\mathbf{G}^{t} + \mathbf{C}_{\mathrm{D}}\right)^{-1}\mathbf{G}\mathbf{C}_{\mathrm{M}}. \tag{A4}$$

A2. Implementation

For each inversion, we assemble a data vector $\mathbf{d}_{\mathrm{obs}}$ by concatenating data from several constant strain rate experiments conducted under different confining pressures, and several brittle creep experiments conducted under different imposed axial stresses. The constant strain rate data consists of time series of axial stress complemented by the peak axial stress and the corresponding axial strain that was reached in each experiment. By assigning a lower uncertainty (in $\mathbf{C}_{d}$) on the peak axial stress and strain relative to the uncertainty on the stress time series, we can assign more weight to this constraint. Doing so helps favor models that accurately predict the position of the peak stress. The brittle creep data for Darley Dale sandstone consist of concatenated time series of axial strain rate from experiments conducted under different axial stresses. Because such data was not available for Westerly granite, we instead concatenated measurements of the representative secondary creep strain rate from experiments conducted under different axial stresses.

At every step of the inversion algorithm, a vector of "simulated data" $\mathbf{d}_{n} = \mathbf{g}(\mathbf{m}_{n})$ is built by simulating each individual experiment, and ordering the outputs to match the order of $\mathbf{d}_{\mathrm{obs}}$. In order to simulate brittle creep, the axial stress is first raised by imposing a constant strain rate matching that of the experiment (e.g., loading up to the star in Figure 4a as damage accumulates in Figure 4b). The damage state achieved by the sample is then used as initial condition for the brittle creep simulation. The axial stress is kept constant as we simulate the evolution of axial strain rates (See Section 3).

To ensure that the inversion does not assign negative values to parameters which are inherently positive, we construct a model vector $\mathbf{m}$ that contains the logarithm of each SCAM parameter, namely: G_0, γ, μ, a, D_0, D_i, n, K_{IC}, and $\dot{l}_0$. The associated uncertainties (prior or posterior) are thus log-normal distributions of the parameters, or Gaussian distributions of the logarithm of the parameters. If a positive parameter has a standard deviation $\bar{s}$ and a median $\bar{m}$, the distribution of its logarithm can be adequately represented by a Gaussian distribution centered on $\log(\bar{m})$ with variance $\bar{\sigma}^2 = \log\left(1 + \bar{s}^2/\bar{m}^2\right)$. We make use of these formula to assign uncertainties on the experimental data and on our prior knowledge of the model parameters.

Appendix B: Derivation of the Plastic Viscosity

Two situations have to be considered to construct the plastic viscosity term η_p used in SCAM numerical simulations. The first situation is stresses that lie above the plastic yield envelope at the onset of plastic behavior. This can happen because damage build-up may cause stresses to increase past the plastic yield stress (σ_y). In this case, we require the plastic viscosity to relax excess stresses above σ_y in one iteration. Equation 38 recast in term of $\dot{s}_{ij}$ thus becomes

$$\dot{s}_{ij} = \frac{s_{ij}^{y} - s_{ij}}{\Delta t} = 2G_0\,\mathrm{f}(D)\left(\dot{e}_{ij} - \frac{s_{ij}}{2\eta_p}\right), \tag{B1}$$

where s_{ij}^{y} corresponds to any deviatoric stress tensor whose second invariant satisfies $s_{II}^{y} = \sigma_y$. We approximate Equation B1 by using σ_y, s_{II} and the second invariant of the strain rate tensors $\dot{e}_{II} = \sqrt{J_2(\dot{e})}$:

$$\frac{\sigma_y - s_{II}}{\Delta t} = 2G_0\,\mathrm{f}(D)\left(\dot{e}_{II} - \frac{s_{II}}{2\eta_p}\right). \tag{B2}$$

This yields the following closed form equation for η_p:

$$\eta_p = \frac{s_{II}}{2\left(\dot{e}_{II} - \frac{\sigma_y - s_{II}}{2G_0\,\mathrm{f}(D)\Delta t}\right)}. \tag{B3}$$

The other possible situation involves stresses capped by the yield envelope (i.e., $s_{II} < \sigma_y$). In this case, we additionally require that η_p be infinite if the elastic stress rate $2G_0 \, \mathrm{f}(D)\dot{e}_{II}$ is lower than the value required to reach the yield stress in one iteration $\left(\frac{\sigma_y - s_{II}}{\Delta t}\right)$. This amounts to rewriting η_p:

$$\eta_p = \frac{s_{II}}{2\left(\dot{e}_{II} - \min\left(\frac{\sigma_y - s_{II}}{2G_0 \, \mathrm{f}(D)\Delta t}, \dot{e}_{II}\right)\right)},$$

(B4)

to ensure that the plastic viscosity is finite only when $s_{II} \geq \sigma_y$, or if an elastic stress increment suddenly brings s_{II} above σ_y.

Notation

Mohr-Coulomb plasticity

μ   friction coefficient

ϕ   ($= \arctan \mu$) friction angle on shear defects (ϕ_m at macroscopic scale)

C_m   (macroscopic) cohesion

σ_y   yield stress

$\sigma_y^{(\mathrm{max})}$ intact plastic yield stress (determined by μ_{max} and C_{max})

μ_{max}   initial friction coefficient (in strain weakened Mohr-Coulomb plasticity)

C_{max}   initial cohesion (in strain weakened Mohr-Coulomb plasticity)

$\sigma_y^{(\mathrm{min})}$ fully weakened plastic yield stress (determined by μ_{min} and C_{min})

μ_{min}   fully weakened friction coefficient

C_{min}   fully weakened cohesion

Δe_{II}^p   accumulated plastic strain needed to fully weaken the frictional properties

Damage mechanics

D $\in [D_0, 1]$ damage internal state variable

D_0 $\in [0, 1]$ damage value corresponding to no tensile defect in the rock

D_i   initial damage

D_c   critical damage at the transition between the isolated crack regime and the interacting crack regime

γ $= \mathrm{f}(D = 1)$ ratio of residual over reference shear modulus

N_v   number of shear defects per unit volume

V_c   characteristic volume per crack ($1/N_v$)

A_c   characteristic area per crack

A_b   average area that separates neighboring cracks (bulk area in the (σ_1, σ_2) plane)

ψ   shear defect angle with respect to σ_1

α $\cos \psi$

a   shear defect radius

l   tensile "wing" crack length

K_I   mode I stress intensity factor

$K_I^{(w)}$	mode I stress intensity factor due to the wedging force F_w
$K_I^{(\sigma_3)}$	mode I stress intensity factor due to σ_3
$K_I^{(i)}$	mode I stress intensity factor due to interactions between cracks
σ_3^i	internal stress acting in the direction of σ_3 resulting from cracks interaction
K_{IC}	mode I fracture toughness
$\dot{l}_0$	characteristic crack growth rate
n	Charles law exponent (corrosion index)
β	geometric regularization factor
A_1, A_3	constants that depend on friction and the orientation of shear defects

Stresses and strains

ε_{ij}	strain tensor
σ_1	most compressive principal stress
σ_3	least compressive principal stress
$\Delta\sigma$	$= \sigma_3 - \sigma_1$, differential stress
$\Delta\sigma^c$	differential stress at $K_I = 0$ and $D = D_0$
$\Delta\sigma_{bc}$	Minimum brittle strength
P	$= -\sigma_{kk}/3$ pressure
p_c	$= -\sigma_3$ confining pressure in experiments
e_{ij}	deviatoric strain tensor
s_{ij}	deviatoric stress tensor
e_{ax}	deviatoric axial strain
s_{ax}	deviatoric axial stress
$J_2(X)$	$= (\text{dev}(X_{ij})\text{dev}(X_{ij}))/2$ second invariant of the deviator of second order tensor X
s_{II}	$= \sqrt{J_2(\sigma_{ij})}$ scalar shear stress magnitude
s_{ij}^y	deviatoric stress tensor satisfying the Mohr-Coulomb yield criterion
e_{II}	$= \sqrt{J_2(\varepsilon_{ij})}$ scalar shear strain magnitude
ε_{ij}^p	plastic strain tensor

Additional notations

G	effective shear modulus
G_0	$= G(D = D_0)$ reference shear modulus corresponding to the lowest damage state (no tensile defect)
$f(D)$	weakening function
ν	Poisson's ratio
η_D	damage viscosity
η_p	plastic viscosity (2-D SCAM simulations)
η_{eff}	effective viscosity (2-D SCAM simulations)

η_{min}	minimum viscosity (2-D SCAM simulations)
η_{max}	maximum viscosity (2-D SCAM simulations)
v_i	Components of the velocity field
ρ	density
g_i	Components of the gravity field
Δt	time step

Data Availability Statement

The codes used to produce the results of Section 3 (0-D, written in Julia) and Sections 4 and 6 (2-D, written in MATLAB) are provided in a Zenodo repository (Petit & Olive, 2024).

References

Aben, F. M., Brantut, N., Mitchell, T. M., & David, E. C. (2019). Rupture energetics in crustal rock from laboratory-scale seismic tomography. *Geophysical Research Letters*, *46*(13), 7337–7344. https://doi.org/10.1029/2019GL083040

Arthur, J., Dunstan, T., Al-Ani, Q. A. J. L., & Assadi, A. (1977). Plastic deformation and failure in granular media. *Géotechnique*, *27*(1), 53–74. https://doi.org/10.1680/geot.1977.27.1.53

Ashby, M. F., & Hallam, S. D. (1986). The failure of brittle solids containing small cracks under compressive stress states. *Acta Metallurgica*, *34*(3), 497–510. https://doi.org/10.1016/0001-6160(86)90086-6

Ashby, M. F., & Sammis, C. G. (1990). The damage mechanics of brittle solids in compression. *Pure and Applied Geophysics PAGEOPH*, *133*(3), 33–521. https://doi.org/10.1007/bf00878002

Atkinson, B. K. (1979). A fracture mechanics study of subcritical tensile cracking of quartz in wet environments. *Pure and Applied Geophysics PAGEOPH*, *117*(5), 1011–1024. https://doi.org/10.1007/bf00876082

Atkinson, B. K. (1984). Subcritical crack growth in geological materials. *Journal of Geophysical Research*, *89*(B6), 4077–4114. https://doi.org/10.1029/JB089iB06p04077

Baud, P., & Meredith, P. (1997). Damage accumulation during triaxial creep of Darley Dale sandstone from pore volumometry and acoustic emission. *International Journal of Rock Mechanics and Mining Sciences*, *34*(3–4), 24–el. https://doi.org/10.1016/s1365-1609(97)00060-9

Baud, P., Schubnel, A., & Wong, T.-f. (2000). Dilatancy, compaction, and failure mode in Solnhofen limestone. *Journal of Geophysical Research*, *105*(B8), 19289–19303. https://doi.org/10.1029/2000JB900133

Bhat, H. S., Rosakis, A. J., & Sammis, C. G. (2012). A micromechanics based constitutive model for brittle failure at high strain rates. *Journal of Applied Mechanics*, *79*(3), 031016. https://doi.org/10.1115/1.4005897

Bhat, H. S., Sammis, C., & Rosakis, A. (2011). The micromechanics of westerley granite at large compressive loads. *Pure and Applied Geophysics*, *168*(12), 2181–2198. https://doi.org/10.1007/s00024-011-0271-9

Brace, W. F., & Kohlstedt, D. L. (1980). Limits on lithospheric stress imposed by laboratory experiments. *Journal of Geophysical Research*, *85*(B11), 6248–6252. https://doi.org/10.1029/JB085iB11p06248

Brace, W. F., Paulding, B. W., & Scholz, C. (1966). Dilatancy in the fracture of crystalline rocks. *Journal of Geophysical Research*, *71*(16), 3939–3953. https://doi.org/10.1029/JZ071i016p03939

Brantut, N., Baud, P., Heap, M. J., & Meredith, P. G. (2012). Micromechanics of brittle creep in rocks: Micromechanics of brittle creep. *Journal of Geophysical Research*, *117*(B8). https://doi.org/10.1029/2012JB009299

Brantut, N., Heap, M., Meredith, P., & Baud, P. (2013). Time-dependent cracking and brittle creep in crustal rocks: A review. *Journal of Structural Geology*, *52*, 17–43. https://doi.org/10.1016/j.jsg.2013.03.007

Buck, W. R. (1991). Modes of continental lithospheric extension. *Journal of Geophysical Research*, *96*(B12), 20161–20178. https://doi.org/10.1029/91JB01485

Budiansky, B., & O'connell, R. J. (1976). Elastic moduli of a cracked solid. *International Journal of Solids and Structures*, *12*(2), 81–97. https://doi.org/10.1016/0020-7683(76)90044-5

Byerlee, J. D. (1967). Frictional characteristics of granite under high confining pressure. *Journal of Geophysical Research*, *72*(14), 3639–3648. https://doi.org/10.1029/JZ072i014p03639

Byerlee, J. D. (1978). Friction of rocks. *Pure and Applied Geophysics PAGEOPH*, *116*, 615–626.

Carter, N., Anderson, D. A., Hansen, F. D., & Kranz, R. L. (1981). Creep and creep rupture of granitic rocks. In *Washington DC American Geophysical Union Geophysical Monograph Series* (Vol. 24, pp. 61–82).

Charles, R. J. (1958). Static Fatigue of Glass. I. *Journal of Applied Physics*, *29*(11), 1549–1553. https://doi.org/10.1063/1.1722991

Costin, L. (1983). A microcrack model for the deformation and failure of brittle rock. *Journal of Geophysical Research*, *88*(B11), 9485–9492. https://doi.org/10.1029/JB088iB11p09485

Costin, L. (1985). Damage mechanics in the post-failure regime. *Mechanics of Materials*, *4*(2), 149–160. https://doi.org/10.1016/0167-6636(85)90013-4

Darot, M., & Gueguen, Y. (1986). Slow crack growth in minerals and rocks: Theory and experiments. *Pure and Applied Geophysics PAGEOPH*, *124*(4–5), 677–692. https://doi.org/10.1007/BF00879604

Deshpande, V., & Evans, A. (2008). Inelastic deformation and energy dissipation in ceramics: A mechanism-based constitutive model. *Journal of the Mechanics and Physics of Solids*, *56*(10), 3077–3100. https://doi.org/10.1016/j.jmps.2008.05.002

Dey, T. N., & Wang, C.-Y. (1981). Some mechanisms of microcrack growth and interaction in compressive rock failure. *International Journal of Rock Mechanics and Mining Sciences & Geomechanics Abstracts*, *18*(3), 199–209. https://doi.org/10.1016/0148-9062(81)90974-8

Duretz, T., Borst, R., & Yamato, P. (2021). Modeling lithospheric deformation using a compressible Visco-Elasto-Viscoplastic rheology and the effective viscosity approach. *Geochemistry, Geophysics, Geosystems*, *22*(8). https://doi.org/10.1029/2021GC009675

Eppes, M.-C., & Keanini, R. (2017). Mechanical weathering and rock erosion by climate-dependent subcritical cracking. *Reviews of Geophysics*, *55*(2), 470–508. https://doi.org/10.1002/2017RG000557

Gallen, S. F., Clark, M. K., & Godt, J. W. (2015). Coseismic landslides reveal near-surface rock strength in a high-relief, tectonically active setting. *Geology*, *43*(1), 11–14. https://doi.org/10.1130/G36080.1

Gerya, T. (2010). *Introduction to numerical geodynamic modelling*. Cambridge University Press.

Gerya, T., & Yuen, D. A. (2003). Characteristics-based marker-in-cell method with conservative finite-differences schemes for modeling geological flows with strongly variable transport properties. *Physics of the Earth and Planetary Interiors*, *140*(4), 293–318. https://doi.org/10.1016/j.pepi.2003.09.006

Gratier, J.-P., Dysthe, D. K., & Renard, F. (2013). The role of pressure solution creep in the ductility of the Earth's upper crust. *Advances in Geophysics*, *54*, 47–179. https://doi.org/10.1016/B978-0-12-380940-7.00002-0

Hamiel, Y., Liu, Y., Lyakhovsky, V., Ben-Zion, Y., & Lockner, D. (2004). A viscoelastic damage model with applications to stable and unstable fracturing. *Geophysical Journal International*, *159*(3), 1155–1165. https://doi.org/10.1111/j.1365-246X.2004.02452.x

Heap, M. J., Baud, P., Meredith, P. G., Bell, A. F., & Main, I. G. (2009). Time-dependent brittle creep in Darley Dale sandstone. *Journal of Geophysical Research*, *114*(B7), B07203. https://doi.org/10.1029/2008JB006212

Kachanov, M. L. (1982a). A microcrack model of rock inelasticity part I: Frictional sliding on microcracks. *Mechanics of Materials*, *1*(1), 19–27. https://doi.org/10.1016/0167-6636(82)90021-7

Kachanov, M. L. (1982b). Microcrack model of rock inelasticity part III: Time-dependent growth of microcracks. *Mechanics of Materials*, *1*(2), 123–129. https://doi.org/10.1016/0167-6636(82)90040-0

Kachanov, M. L. (1982c). A microcrack model of rock inelasticity part II: Propagation of microcracks. *Mechanics of Materials*, *1*(1), 29–41. https://doi.org/10.1016/0167-6636(82)90022-9

Kachanov, M. L. (1993). Elastic solids with many cracks and related problems. *Advances in Applied Mechanics*, *30*, 259–445. https://doi.org/10.1016/S0065-2156(08)70176-5

Karabulut, H., & Bouchon, M. (2007). Spatial variability and non-linearity of strong ground motion near a fault. *Geophysical Journal International*, *170*(1), 262–274. https://doi.org/10.1111/j.1365-246X.2007.03406.x

Karrech, A., Regenauer-Lieb, K., & Poulet, T. (2011). A damaged visco-plasticity model for pressure and temperature sensitive geomaterials. *International Journal of Engineering Science*, *49*(10), 1141–1150. https://doi.org/10.1016/j.ijengsci.2011.05.005

Kaus, B. J. (2010). Factors that control the angle of shear bands in geodynamic numerical models of brittle deformation. *Tectonophysics*, *484*(1–4), 36–47. https://doi.org/10.1016/j.tecto.2009.08.042

Kranz, R. L. (1979). Crack growth and development during creep of Barre granite. *International Journal of Rock Mechanics and Mining Sciences & Geomechanics Abstracts*, *16*(1), 23–35. https://doi.org/10.1016/0148-9062(79)90772-1

Lavier, L. L., & Buck, W. R. (2002). Half graben versus large-offset low-angle normal fault: Importance of keeping cool during normal faulting. *Journal of Geophysical Research*, *107*(B6), ETG–8. https://doi.org/10.1029/2001jb000513

Lavier, L. L., Buck, W. R., & Poliakov, A. N. B. (2000). Factors controlling normal fault offset in an ideal brittle layer. *Journal of Geophysical Research*, *105*(B10), 23431–23442. https://doi.org/10.1029/2000JB900108

Lemiale, V., Mühlhaus, H.-B., Moresi, L., & Stafford, J. (2008). Shear banding analysis of plastic models formulated for incompressible viscous flows. *Physics of the Earth and Planetary Interiors*, *171*(1–4), 177–186. https://doi.org/10.1016/j.pepi.2008.07.038

Le Pourhiet, L. (2013). Strain localization due to structural softening during pressure sensitive rate independent yielding. *Bulletin de la Societe Geologique de France*, *184*(4–5), 357–371. https://doi.org/10.2113/gssgfbull.184.4-5.357

Lockner, D. A. (1998). A generalized law for brittle deformation of Westerly granite. *Journal of Geophysical Research*, *103*(B3), 5107–5123. https://doi.org/10.1029/97JB03211

Lockner, D. A., Byerlee, J. D., Kuksenko, V., Ponomarev, A., & Sidorin, A. (1991). Quasi-static fault growth and shear fracture energy in granite. *Nature*, *350*(6313), 39–42. https://doi.org/10.1038/350039a0

Lyakhovsky, V., Ben-Zion, Y., & Agnon, A. (1997). Distributed damage, faulting, and friction. *Journal of Geophysical Research*, *102*(B12), 27635–27649. https://doi.org/10.1029/97JB01896

Manaker, D. M., Turcotte, D. L., & Kellogg, L. H. (2006). Flexure with damage. *Geophysical Journal International*, *166*(3), 1368–1383. https://doi.org/10.1111/j.1365-246X.2006.03067.x

Marrett, R., Ortega, O. J., & Kelsey, C. M. (1999). Extent of power-law scaling for natural fractures in rock. *Geology*, *27*(9), 799. https://doi.org/10.1130/0091-7613(1999)027⟨0799:EOPLSF⟩2.3.CO;2

McBeck, J., Kandula, N., Aiken, J. M., Cordonnier, B., & Renard, F. (2019). Isolating the factors that govern fracture development in rocks throughout dynamic in situ X-ray tomography experiments. *Geophysical Research Letters*, *46*(20), 11127–11135. https://doi.org/10.1029/2019GL084613

Menéndez, B., Zhu, W., & Wong, T.-F. (1996). Micromechanics of brittle faulting and cataclastic flow in Berea sandstone. *Journal of Structural Geology*, *18*(1), 1–16. https://doi.org/10.1016/0191-8141(95)00076-P

Meyer, S. E., Kaus, B. J. P., & Passchier, C. (2017). Development of branching brittle and ductile shear zones: A numerical study. *Geochemistry, Geophysics, Geosystems*, *18*(6), 2054–2075. https://doi.org/10.1002/2016GC006793

Molnar, P., Anderson, R. S., & Anderson, S. P. (2007). Tectonics, fracturing of rock, and erosion. *Journal of Geophysical Research*, *112*(F3). https://doi.org/10.1029/2005JF000433

Moresi, L., Dufour, F., & Mühlhaus, H.-B. (2003). A Lagrangian integration point finite element method for large deformation modeling of viscoelastic geomaterials. *Journal of Computational Physics*, *184*(2), 476–497. https://doi.org/10.1016/S0021-9991(02)00031-1

Morley, C. K. (1996). Discussion of potential errors in fault heave methods for extension estimates in rifts, with particular reference to fractal fault populations and inherited fabrics. *Geological Society, London, Special Publications*, *99*(1), 117–134. https://doi.org/10.1144/GSL.SP.1996.099.01.10

Naliboff, J. B., Glerum, A., Brune, S., Péron-Pinvidic, G., & Wrona, T. (2020). Development of 3-d rift heterogeneity through fault network evolution. *Geophysical Research Letters*, *47*(13), e2019GL086611. https://doi.org/10.1029/2019GL086611

Nemat-Nasser, S., & Horii, H. (1982). Compression-induced nonplanar crack extension with application to splitting, exfoliation, and rockburst. *Journal of Geophysical Research*, *87*(B8), 6805–6821. https://doi.org/10.1029/JB087iB08p06805

Olive, J.-A., Behn, M. D., Mittelstaedt, E., Ito, G., & Klein, B. Z. (2016). The role of elasticity in simulating long-term tectonic extension. *Geophysical Journal International*, *205*(2), 728–743. https://doi.org/10.1093/gji/ggw044

Pan, S., Naliboff, J., Bell, R., & Jackson, C. (2022). Bridging spatiotemporal scales of normal fault growth during continental extension using high-resolution 3d numerical models. *Geochemistry, Geophysics, Geosystems*, *23*(7), e2021GC010316. https://doi.org/10.1029/2021GC010316

Pan, S., Naliboff, J., Bell, R., & Jackson, C. (2023). How do rift-related fault network distributions evolve? Quantitative comparisons between natural fault observations and 3d numerical models of continental extension. *Tectonics*, *42*(10), e2022TC007659. https://doi.org/10.1029/2022TC007659

Paterson, M. S., & Wong, T.-F. (2005). In *Experimental rock deformation: The brittle field* (Vol. 348). Springer.

Perol, T., & Bhat, H. S. (2016). Micromechanics-based permeability evolution in brittle materials at high strain rates. *Pure and Applied Geophysics*, *173*(8), 2857–2868. https://doi.org/10.1007/s00024-016-1354-4

Petit, L., & Olive, J.-A. (2024). A sub-critically altered Maxwell (SCAM) constitutive law for brittle rocks: January 6, 2024 release (version 2.0) [Software]. *Zenodo*. https://doi.org/10.5281/zenodo.10464422

Poliakov, A. N. B., & Buck, W. R. (1998). Mechanics of stretching elastic-plastic-viscous layers: Applications to slow-spreading mid-ocean ridges. In W. Roger Buck, P. T. Delaney, J. A. Karson, & Y. Lagabrielle (Eds.), *Geophysical Monograph Series* (pp. 305–324). American Geophysical Union.

Rackauckas, C., & Nie, Q. (2017). DifferentialEquations.jl—A performant and feature-rich ecosystem for solving differential equations in Julia. *Journal of Open Research Software*, *5*(1), 15. https://doi.org/10.5334/jors.151

Rudnicki, J., & Rice, J. (1975). Conditions for the localization of deformation in pressure-sensitive dilatant materials. *Journal of the Mechanics and Physics of Solids*, *23*(6), 371–394. https://doi.org/10.1016/0022-5096(75)90001-0

Sammis, C. G., & Ashby, M. F. (1986). The failure of brittle porous solids under compressive stress states. *Acta Metallurgica*, *34*(3), 511–526. https://doi.org/10.1016/0001-6160(86)90087-8

Scholz, C., Dawers, N., Yu, J.-Z., Anders, M., & Cowie, P. (1993). Fault growth and fault scaling laws: Preliminary results. *Journal of Geophysical Research*, *98*(B12), 21951–21961. https://doi.org/10.1029/93jb01008

Spiegelman, M., May, D. A., & Wilson, C. R. (2016). On the solvability of incompressible Stokes with viscoplastic rheologies in geodynamics: Issues in viscoplasticity. *Geochemistry, Geophysics, Geosystems*, *17*(6), 2213–2238. https://doi.org/10.1002/2015GC006228

Tada, H., Paris, P. C., & Irwin, G. R. (1973). The stress analysis of cracks. *Handbook, Del Research Corporation*, *34*, 635.

Tapponnier, P., & Brace, W. F. (1976). Development of stress-induced microcracks in Westerly granite. *International Journal of Rock Mechanics and Mining Sciences & Geomechanics Abstracts*, *13*(4), 103–112.

Tarantola, A. (2005). Inverse problem theory and methods for model parameter estimation. *Society for Industrial and Applied Mathematics*. https://doi.org/10.1137/1.9780898717921

Thomas, M. Y., Bhat, H. S., & Klinger, Y. (2017). Effect of brittle off-fault damage on earthquake rupture dynamics. In M. Y. Thomas, T. M. Mitchell, & H. S. Bhat (Eds.), *Geophysical Monograph Series* (pp. 255–280). John Wiley & Sons, Inc. https://doi.org/10.1002/9781119156895.ch14

Tsitouras, C., Simos, T. E., Psihoyios, G., & Tsitouras, C. (2009). Runge-Kutta pairs of orders 5(4) using the minimal set of simplifying assumptions. In *AIP Conference Proceedings* (pp. 69–72). Rethymno, Crete (Greece): AIP. https://doi.org/10.1063/1.3241561

Vermeer, P. A., & De Borst, R. (1984). Non-associated plasticity for soils, concrete and rock. *Heron*, *29*(3).

Walsh, J. B. (1965a). The effect of cracks on the compressibility of rock. *Journal of Geophysical Research*, *70*(2), 381–389. https://doi.org/10.1029/JZ070i002p00381

Walsh, J. B. (1965b). The effect of cracks on the uniaxial elastic compression of rocks. *Journal of Geophysical Research*, *70*(2), 399–411. https://doi.org/10.1029/JZ070i002p00399

Wang, X.-Q., Schubnel, A., Fortin, J., Guéguen, Y., & Ge, H.-K. (2013). Physical properties and brittle strength of thermally cracked granite under confinement: Strength of thermally cracked granite. *Journal of Geophysical Research: Solid Earth*, *118*(12), 6099–6112. https://doi.org/10.1002/2013JB010340

Wawersik, W. R., & Brace, W. F. (1971). Post-failure behavior of a granite and diabase. *Rock Mechanics Felsmechanik Mcanique des Roches*, *3*(2), 61–85. https://doi.org/10.1007/BF01239627

Wu, C., Peng, Z., & Ben-Zion, Y. (2009). Non-linearity and temporal changes of fault zone site response associated with strong ground motion. *Geophysical Journal International*, *176*(1), 265–278. https://doi.org/10.1111/j.1365-246X.2008.04005.x

Wu, X., Baud, P., & Wong, T. (2000). Micromechanics of compressive failure and spatial evolution of anisotropic damage in Darley Dale sandstone. *International Journal of Rock Mechanics and Mining Sciences*, *37*(1–2), 143–160. https://doi.org/10.1016/S1365-1609(99)00093-3

Zhang, J., Wong, T.-F., & Davis, D. M. (1990). Micromechanics of pressure-induced grain crushing in porous rocks. *Journal of Geophysical Research*, *95*(B1), 341–352. https://doi.org/10.1029/JB095iB01p00341

Zoback, M. D., & Byerlee, J. D. (1975). The effect of microcrack dilatancy on the permeability of westerly granite. *Journal of Geophysical Research*, *80*(5), 752–755. https://doi.org/10.1029/JB080i005p00752